Title

Coupled modeling of hydrogeochemical and electrical resistivity data for exploring the impact of recharge on subsurface contamination

Journal

Water Resources Research, 47(W02509)

Authors

Kowalsky, M.B.
Gasperikova, E.
Finsterle, S.
et al.

Publication Date

2011-04-01

Coupled modeling of hydrogeochemical and electrical resistivity data for exploring the impact of recharge on subsurface contamination

M.B. Kowalsky,[1] E. Gasperikova,[1] S. Finsterle,[1] D. Watson,[2] G. Baker,[3] and S.S. Hubbard[1]

[1]*Earth Sciences Division, Lawrence Berkeley National Laboratory, Berkeley, CA*

[2]*Environmental Sciences Division, Oak Ridge National Laboratory, Oak Ridge, TN*

[3]*Department of Geological Sciences, University of Tennessee, Knoxville, TN*

Abstract

The application of geophysical methods, in particular electrical resistivity measurements, may be useful for monitoring subsurface contamination. However, interpreting geophysical data without additional data, and without considering the associated hydrogeochemical processes, is challenging since the geophysical response is sensitive to not only heterogeneity in rock properties, but also to the saturation and chemical composition of pore fluids. We present an inverse modeling framework that incorporates the simulation of hydrogeochemical processes and time-lapse electrical resistivity data, and apply it to various borehole and cross-borehole datasets collected in 2008 near the S-3 Ponds at the DOE Oak Ridge Integrated Field Research Challenge site, where efforts are underway to better understand freshwater recharge and associated contaminant dilution. Our goal is to show the coupled hydrogeochemical-geophysical modeling framework can be used to a) develop a model that honors all the available datasets, b) help understand the response of the geophysical data to subsurface properties and processes at the site and c) allow for the estimation of petrophysical parameters needed for interpreting the

geophysical data. We present a series of cases involving different datasets and increasingly complex models, and find that the approach provides useful information about soil properties, recharge-related transport processes, and the geophysical response. Spatial heterogeneity of the petrophysical model can be described sufficiently with two layers, and its parameters can be estimated concurrently with the hydrogeochemical parameters. For successful application of the approach, the parameters of interest must be sensitive to the available data, and the experimental conditions must be carefully modeled.

1. Introduction

The high value of geophysical data for hydrological investigations—in the field broadly referred to as hydrogeophysics—is increasingly recognized due to the sensitivity of geophysical measurements to properties that are (directly or indirectly) related to hydrological processes. The challenge is in extracting information from geophysical data that can be used quantitatively to gain insight into the spatiotemporal nature of hydrogeochemical processes and to inform hydrological models. The application of electrical resistivity measurements in particular may be useful for monitoring subsurface contamination, but interpreting those measurements without additional data, and without considering the associated hydrogeochemical processes is challenging since the electrical response is sensitive to not only heterogeneity in soil and rock properties, but also to the temporally varying saturation and the chemical composition of pore fluids. In general, the geophysical response to hydrological processes and parameters must be understood before such data can be applied widely at a given site. Conversely, if a quantitative understanding can be gained, geophysical data may be useful not just for imaging the subsurface, but also for the estimating hydrological and geochemical parameters.

One way to integrate different types of hydrogeophysical data is through coupled hydrological-geophysical modeling such that simulated geophysical measurements become a function of the hydrological processes. This modeling approach, also referred to as coupled hydrogeophysical modeling, is useful in "forward mode" to evaluate the sensitivity of different geophysical measurements for monitoring hydrological processes [*Kowalsky et al.*, 2009]. The approach is also useful in "inverse mode," wherein an optimization algorithm is used to determine the relevant hydrological parameters that minimize the difference between measured and simulated geophysical and hydrological data.

An important benefit of the coupled hydrogeophysical approach is that it only requires the simulation of the directly measured geophysical attributes (e.g., GPR travel times) instead of the results of a computationally expensive tomographic inversion [e.g., *Peterson et al.*, 1985] to obtain geophysical images at each survey time for every set of parameters considered in the iterative inversion procedure. Furthermore, errors that might otherwise be introduced in the tomographic inversion [*Day-Lewis and Lane*, 2004] are excluded in the coupled hydrogeophysical approach.

The coupled hydrogeophysical approach is most commonly applied to systems in which the physical properties (e.g., water saturation, solute concentration, pressure, temperature) are undergoing transient changes, and time-lapse geophysical measurements are available that are sensitive to those changes. It is also possible to apply such an approach to hydrological systems that are at steady state [*Cassiani and Binley*, 2005], although in general the geophysical data may be less sensitive to the hydrological properties (relative to time-lapse data collected during transient conditions).

Johnson et al. [2009] discuss the advantages and limitations of some choices for implementing geophysical data in approaches that rely on a petrophysical transformation between geophysical and hydrological properties. They propose an alternative formulation that takes advantage of correlation between changes in geophysical and hydrological properties and bypasses the need for a petrophysical model. *Hinnell et al.* [2010] compare the abilities of coupled and uncoupled inversion using an example based on the use of surface-based electrical conductivity surveys for monitoring water infiltration and redistribution. Evaluating the merits of joint inversion approaches for different hydrological applications remains an active area of research. Many such studies have focused on synthetic studies rather than field-based investigations, and the results are likely to be application specific.

An example of the coupled hydrogeophysical modeling framework involves the use of time-lapse ground penetrating radar (GPR) measurements, which are primarily sensitive to variations in the dielectric constant, to indirectly estimate the heterogeneous distribution of permeability and parameters of the relative permeability and capillary pressure functions [*Kowalsky et al.*, 2004, 2005; *Finsterle and Kowalsky*, 2008]. This is made possible by the dependence of the dielectric constant on water saturation. A hydrological forward model (which simulates the evolution of water saturation) and a GPR forward model (which simulates GPR travel times as a function of dielectric constant, which depends on the water saturation, porosity, and temperature) are coupled such that the simulated hydrological and geophysical measurements become a function of the unknown hydrological parameters. The hydrological parameters can then be estimated in an inverse modeling framework. Furthermore, they show that estimating a parameter of the petrophysical function helps to overcome uncertainty in the petrophysical relationship. A related application invoked the coupled simulation of unsaturated flow and off-

ground GPR measurements for estimating near-surface hydrological parameters [*Lambot et al.*, 2006; *Jadoon et al.*, 2008]. Other studies illustrated the usefulness of GPR measurements for inferring hydrological properties using a variety of approaches [e.g., *Binley et al.*, 2002; *Rucker and Ferré*, 2004, *Farmani et al.*, 2008].

Electrical resistivity measurements are another type of geophysical data that are well established for monitoring subsurface properties. They have been used to monitor, for example, hydrological barriers [*Daily and Ramirez*, 2000], leakage from underground tanks [*Ramirez et al.*, 1996], remediation processes [*Ramirez et al.*, 1993; *Daily and Ramirez*, 1995], as well as the movement of water or dissolved solutes in the subsurface [*Daily et al.*, 1992; *Park*, 1998; *Slater et al.*, 2000; *Binley et al.*, 2002; *French et al.*, 2002; *Kemna et al.*, 2002; Singha and Gorelick, 2008], and changes in subsurface water content due to rainfall [*Zhou et al.*, 2001]. A stochastic data integration approach combined electrical resistivity data and other hydrological datasets to improve estimates of water saturation [*Yeh et al.*, 2002].

A variety of applications that include the use of electrical resistivity data have been proposed for inferring hydrological parameters, sometimes in combination with other data. For example, *Kemna et al.* [2002] used time-varying distributions of solute concentration that were inferred from time-lapse electrical resistance tomography (ERT) to parameterize an equivalent convection-dispersion model [*Kemna et al.*, 2002]. *Binley et al.* [2002] carried out calibration of a hydrological model using GPR and ERT data, as did *Looms et al.* [2006] and *Deiana et al.* [2008]. *Looms et al*. [2008] demonstrated that the combination of different geophysical data types can decrease uncertainty in hydrological parameters when integrated within a data fusion approach. *Day-Lewis and Singha* [2008] related the temporal moments of ERT data to parameters of a dual-porosity transport model. *Pollock and Cirpka* [2008] developed a coupled

system for simulating groundwater flow, solute transport, and electrical resistivity measurements with the goal of using moments in a hydrogeophysical inversion.

Electrical resistivity measurements are promising for inclusion in a coupled hydrogeophysical modeling framework [*Ferré et al.*, 2006; *Lehikoinen et al.*, 2009, 2010; *Hinnell et al.*, 2009]. Similar to the dielectric constant in GPR applications, the electrical resistivity of soil is in general not directly related to hydrological parameters such as permeability, but it can be related to a combination of the current system state (specifically saturation and solute concentration, which determines pore fluid electrical conductivity) and soil properties (e.g., clay content, and porosity).

The overall motivation for this study is to begin developing a tool that can be used to gain insight into the impact of recharge on subsurface hydrogeochemical responses over field-scales at the DOE Oak Ridge National Laboratory (ORNL) Integrated Field Research Challenge (IFRC) site. Understanding the impact of freshwater recharge on subsurface contaminant concentration and mobility is a focus of the IFRC research effort. Recharge creates large hydraulic and geochemical gradients in the subsurface at the IFRC site that can disrupt geochemical equilibrium in the groundwater as sub-neutral rainwater (which is high in dissolved oxygen and low in ionic strength) mixes with acidic, high ionic strength groundwater. The oscillations of geochemical conditions in the shallow groundwater are hypothesized to have significant implications for solute transport. Solutes and colloids that adsorb onto aquifer solids can be released into solution by decreases in ionic strength and pH. The decreases in ionic strength also cause thermodynamic undersaturation of the groundwater with respect to some mineral species and may result in mineral dissolution [*van de Hoven et al.*, 2005]. The system response to recharge events is complex because of the large variations in contaminant

concentrations, pH, mineralogy, and due to preferential flowpaths in the plume region. Better understanding the response to recharge is challenging because of the large spatial extent of the plume, the complexity of the subsurface hydrogeochemistry, and the sparseness of direct hydrogeochemical measurements.

We present an inverse modeling framework that incorporates the simulation of hydrogeochemical processes and time-lapse electrical resistivity data, and apply it to datasets collected in 2008 near the S-3 Ponds at the DOE Oak Ridge Integrated Field Research Challenge site, where efforts are underway to better understand freshwater recharge and associated contaminant dilution. We aim to use the coupled hydrogeochemical-geophysical modeling framework to develop a model that a) honors a variety of datasets (time-lapse electrical resistivity data and hydrogeochemical data, including water level data and solute concentration data), b) improves understanding of the response of geophysical data to subsurface properties at the site, and c) allows for estimation of the spatially variable petrophysical parameters that are necessary for interpreting geophysical data collected at the site. After describing the methodology, the experimental site and datasets, and the hydrogeochemical and geophysical models used in the procedure, we present a series of cases in which the approach is applied with different datasets and increasingly complex models.

2. Methodology

The approach used in this study consists of three components: (1) a hydrogeochemical forward model, which simulates fluid flow and solute transport and the corresponding hydrogeochemical measurements; (2) a geophysical forward model, specifically an electrical resistivity forward model, which simulates the injection of electrical current in the subsurface

and the corresponding resistivity measurements; and (3) a hydrogeophysical modeling framework to control the procedure. These components are briefly described in the following sections.

2.1. Hydrogeochemical Forward Model (HM)

The HM used in this study is TOUGH2 [*Pruess et al.*, 1999], which numerically simulates the behavior of multiphase, multicomponent fluid mixtures and heat in porous and fractured geologic formations. While temperature is known to affect the electrical properties of sediment mixtures, the temperature fluctuations were minor for the nine-day period in which electrical resistivity surveys were conducted for this study. In addition, the temperature did not vary significantly with depth in the region sampled by the electrical resistivity measurements. We therefore limit the study to isothermal simulations. The three equations solved per grid block are mass balance equations for the components water, air, and solute (nitrate). We assume the solute is dissolved in the aqueous phase and does not affect the fluid properties (e.g., viscosity and density). Capillary pressure and relative permeability behavior are modeled using the relationships developed by *van Genuchten* [1980].

Some of the directly simulated state variables, such as nitrate concentrations at specified locations and times, are considered as hydrogeochemical measurements. We also simulate hydraulic head (or water level) measurements in the saturated and unsaturated zones at the screened intervals. In addition, the simulated distributions of water saturation and nitrate concentration are used as input for the geophysical forward model (GM), which is described in the next section.

2.2. Geophysical Forward Model (GM)

The GM used in this study is CRMOD [*Kemna*, 2000; *Kemna et al.*, 2002], which simulates the 2D flow of electrical current in the ground and the corresponding resistivity measurements. Input for CRMOD includes electrode configuration information specifying the sets of dipoles in which current is injected and measured. The input resistivity distribution is calculated from properties simulated in the HM based on the petrophysical models described in Section 4.2. In addition to site-specific parameters, the petrophysical model uses the simulated distributions of water saturation and solute concentration, along with the porosity distribution, to calculate the electrical resistivity distributions for the specified geophysical survey times.

In this study we assume that the hydrogeochemical processes being monitored are relatively slow compared to the time required for data collection. For simplicity, we simulate electrical resistivity measurements for a given survey at a single point in time. However, there is no fundamental limitation in our approach that prevents the simulation of individual measurements at precisely recorded times.

It is worth noting that the numerical grids for the HM and GM need not be identical, since output from the HM is mapped onto the GM grid. This is a useful feature since there are many cases in which it is convenient to use different grids (e.g., finer grid spacing may be required for one of the forward models, or the electrical resistivity model may only need to cover a small region of a larger HM domain).

We restrict our analysis to a 2D GM in order to reduce the computational burden otherwise imposed by 3D geophysical simulations.

2.3. Coupled Hydrogeophysical Modeling Framework

We implemented a coupled hydrogeophysical modeling approach in iTOUGH2 [*Finsterle*, 1999; *Finsterle*, 2004], which provides forward and inverse modeling capabilities for a variety of hydrogeochemical and geophysical data (Figure 1). The approach integrates the HM and GM to allow for inverse modeling using the following procedure: (1) a set of hydrogeochemical and geophysical parameters is specified; (2) a hydrogeochemical simulation is performed with the HM, producing the simulated hydrogeochemical data (water levels and nitrate concentrations) and the information used as input for the GM; (3) a petrophysical model translates the HM output (e.g., water saturation, solute concentration, and porosity) into the relevant geophysical property (electrical resistivity); (4) the geophysical data (electrical resistances) are simulated with the GM at the specified geophysical survey times; (5) an objective function is evaluated to measure the misfit between the measured and simulated hydrogeochemical and geophysical data; (6) a new set of hydrological and geophysical parameters is obtained through an optimization algorithm; and (7) the process is repeated starting at (2), until a set of parameters that minimizes the objective function is found.

Aside from its usefulness in performing inverse modeling, the coupled hydrogeophysical modeling framework is helpful for evaluating the sensitivity of different hydrogeophysical data types to the parameters and processes of interest for a particular site [e.g., Kowalsky et al., 2008]. For example, when designing a field experiment, it is useful to perform a sensitivity study to determine the optimal placement of measurements and the sampling frequency, as well as to determine which data types are likely to be most sensitive to the relevant parameters. It is hoped that the coupled model we begin to develop in this work can be used in the future to optimize data collection at the site.

3. Description of Field Experiment at ORNL S-3 Ponds Site

The DOE Oak Ridge IFRC was established to investigate long-term immobilization strategies and to improve the understanding of rates and mechanisms that control contaminant fate and transport from the plot scale to the watershed scale. One of the research objectives of the IFRC is to examine the impact of freshwater recharge on contaminant dilution and mobility, and to explore the use of geophysical methods for assessing associated subsurface hydrogeochemical processes that are often difficult to ascertain using sparse wellbore data alone.

3.1. Site Description

The study site is adjacent to the southern-most corner of the S-3 Ponds at the Oak Ridge Reservation, located in eastern Tennessee (Figure 2). From 1951 to 1983, unlined surface trenches (the S-3 Ponds) received approximately 2.5 million gallons per year of waste containing acidic nitrate and uranium, among other contaminants. After the waste was neutralized, the trenches were capped in 1988 and covered by a parking lot. The majority of the waste originally present in the S-3 Ponds has since migrated into the underlying geological formation and precipitated or adsorbed onto the solid phase, or diffused into the matrix, forming a persistent secondary source of groundwater contamination. Extensive contaminant plumes now emanate from the S-3 Ponds and ultimately discharge to surface water sources, jeopardizing the surrounding ecosystem.

Groundwater recharge at the study site is substantial and highly variable, exerting a major influence on local hydrogeochemical processes. Recharge from precipitation fluctuates not only seasonally and annually, but also varies rapidly in response to individual storm events. A related source of recharge—runoff from the S-3 parking lot—enters the formation through intermittent

standing water in a drainage ditch that surrounds the parking lot. Perched water bodies are suspected to form at shallow depths, also affecting local recharge. Heterogeneity at the S-3 site—comprised of a complex mixture of human-placed fill, soil, Saprolite, and fractured sedimentary rocks—along with preferential flow paths and a rapid aquifer response to fluctuations in recharge, all lead to spatial and temporal variability of groundwater chemistry and contaminant transport [*van de Hoven,* 2005]. Understanding the influence of recharge on contaminant fate in this complex, dynamic environment requires the development of new approaches that integrate multiple types of data.

Chen et al. [2006] conducted a study in a region located approximately 10 m west of the site considered here. Their study, which involved the inversion of flowmeter and crosshole seismic tomography data for hydraulic conductivity zonation, identified a fracture zone with high hydraulic conductivity that varied in thickness and continuity. Assessment of tracer-test data confirmed that heterogeneity at the site (in the fracture zone in particular) heavily impacted local flow and transport.

In this study we focus on the recharge-related dilution of nitrate, which occurs at concentrations up to 50,000 mg/l in the S-3 Ponds area. Note that the nitrate concentrations stated throughout this paper are mg/l NO_3. Although not examined here, the higher pH of rainfall relative to the groundwater leads to desorption of uranium, which is present at the site at concentrations up to 60 mg/l.

It should be noted that we assume dilution is the most dominant process affecting nitrate concentration, especially over the short time frame (during a period of especially high recharge) over which the geochemical data analyzed in this study were collected (13 days). Issues related

to the reactive transport of nitrate at the site are being considered as part of the larger IFRC effort.

3.2. Experimental Setup and Measurements

A measurement campaign was conducted in 2008 to monitor the geophysical responses to recharge events at the study site. The campaign included time-lapse surface and cross-borehole resistivity measurements, collected in conjunction with a variety of hydrogeochemical data. Cross-borehole seismic and surface seismic refraction measurements were also collected at the site, all of which are leading to improved characterization of the subsurface [e.g., *Chen et al.*, 2010; *Gaines et al.*, 2009].

In this study we consider hydrogeophysical datasets collected from several wells near the S-3 Ponds (see Figure 3), including water level data in wells SG002 and FW117 (in the perched and saturated zones, respectively); multilevel geochemistry data in FW120; and cross-borehole electrical resistivity data in wells FW124 and FW125. The rainfall rate for the 2008 measurement period (days 98 to 365, corresponding to April 1 through December 31, 2008) is shown in Figure 4, along with the water level in the drainage ditch next to the site. Note that while individual rainfall events may be short in duration, water typically remains longer in the drainage ditch.

Water level data in wells SG002 and FW117 indicate that recharge is highly variable in time (Figure 5). There is initially water present in the perched zone well (SG002), but the water level decreases until the well becomes dry at day 170 (June 19), after which the perched zone remains mostly dry (except for spikes occurring after several infiltration events) until the onset of winter rainfall starting around day 318 (November 14). Some water level data from SG002 were discarded between days 342 and 352 (between December 8 and 18), because they were affected

by the extraction of water for geochemistry measurements. The water level in the saturated zone well (FW117) also shows significant variability: it decreases rather steadily by approximately one meter from day 98 (April 1) to day 310 (November 6), with the exception of some temporary increases around days 190 (July 9) and 235 (August 23), and then increases dramatically after day 310 with the increased winter rainfall.

Of the geochemistry data collected in FW120, we focus solely on nitrate concentrations, which contribute most significantly to the total dissolved solids at the site. In particular, we focus on nitrate concentration data collected on six days in December (days 343, 344, 346, 349, 351, 356, which correspond to December 9, 10, 12, 15, 17, and 22, respectively), as shown in Figure 6a. Since these data were collected in a period of sustained heavy rainfall and high recharge (see Figure 4), it is not surprising to observe overall nitrate dilution, but it is interesting to note that the level of dilution varies with depth and that in some cases nitrate concentration increases. At the shallowest sampling depth (near 5.5 m), the nitrate concentration remained relatively low (approximately 110 mg/l) and nearly constant, while near 8 m depth, the concentration increased slightly from its initial value of 2176 mg/l, followed by continued decrease, starting after day 346, to 1060 mg/l. In contrast, at 13.2 m the concentration decreased monotonically from 5131 mg/l to 2357 mg/l. The highest concentrations for all times are observed at the deepest sampling depth (15.2 m).

In general, the process for collecting cross-borehole electrical resistivity data is as follows: a number of electrodes are placed in boreholes at desired locations; pairs of electrodes are selected into which current is injected (current dipoles); pairs of electrodes (measurement dipoles) are selected at which measurements are to be made for each current injection dipole; and a multiplexer is programmed for the automatic injection of current and the measurement of

resistance (equal to the recorded voltage divided by the recorded current). A dipole consists of electrodes placed in the same borehole or in opposing boreholes, and the spacing between electrodes can be varied.

For this experiment, a total of 56 electrodes were permanently installed along two boreholes (FW124 and FW125) that were spaced 3 m apart. Vertical spacing between the electrodes is 0.6 m in the upper 10 m and 0.3 m in the transition zone (Figure 7). A complete dataset contains more than 10,000 points measured for various current and measurement dipole combinations. Of all the dipole configurations that were collected, we focused on a subset that was relatively small (and thus manageable) and that we expect to be more sensitive to vertical variations in subsurface properties than to lateral variations. In particular, the chosen subset includes only the current dipoles formed with electrodes in opposing boreholes and the measurement dipoles that are formed by electrodes in the same. Furthermore, only the electrodes that remain in the saturated zone for all survey times are considered. Also, for measurements that were found to be erroneous at any survey time (e.g., for voltages below 0.2 mV and current below 200 mA, corresponding to measurements with suspected contact resistance problems), data from the corresponding dipole configurations were removed for all survey times. One of the current dipoles and corresponding measurement dipoles is depicted in Figure 7a. An additional 19 current dipoles at different depths are included in the study, each with a different set of measurement dipoles, giving a total of 581 measurements per survey (Figure 7b). We consider two surveys performed on day 345 and 354 in December 2008. Two additional surveys were performed on days 346 and 353, but the corresponding data values did not merit inclusion in the inversion, because they were not sufficiently different from the datasets collected on days 345 and 354, respectively.

4. Development of Coupled Hydrogeophysical Model for S-3 Ponds Site

Details of the hydrogeochemical and electrical resistivity simulations are given next (Sections 4.1 and 4.2, respectively), followed by application of the approach to several cases with successively increasing model complexity (Section 4.3).

4.1. Hydrogeochemical Simulations

Our conceptual model for the site is shown in Figure 8a. The modeled region covers a vertical distance of 16 m and a horizontal distance of 20 m. The geological layering includes the atmosphere (at 0 m), a fill layer (0 to 2.6 m), a Saprolite layer (2.6 to 10 m), the so-called transition zone (10 to 16 m), and a low permeability bedrock layer (below 16 m). The transition zone is thought to be less cohesive than the units above and below it and can contain fracture zones with high hydraulic conductivity that serve as preferential pathways [e.g., *Chen et al.*, 2006]. The permeability in the Saprolite has been observed to be several orders of magnitude lower than in the transition zone, and as a consequence, the horizontal groundwater flux in the Saprolite is orders of magnitude lower than in the transition zone. We take advantage of this observation to improve the computational efficiency of the hydrogeochemical model (i.e., by using a 1D grid) for the inversion case (Case A) considered in Section 4.3.1

For the hydrogeochemical simulations, we consider both 1D and 2D numerical representations of the system (Figure 8b and 8c, respectively). The 1D HM accounts for vertical flow in the fill and Saprolite layers and horizontal outflow in the transition zone to a boundary whose pressure is held constant at a value determined in the inversion. In the 1D model, the grid blocks are 20 m wide, and the vertical spacing is 12.5 cm for depths between 0 and 6 m, and 25 cm for depths between 6 and 10 m. The transition zone is represented by a single grid block with

a thickness of 6 m. The upper grid block of the model remains fixed at constant atmospheric pressure.

Note that use of a 1D HM makes the assumption that the hydrogeochemical processes of interest in the fill and Saprolite layers occur predominantly in the vertical direction (or the vertical transport process occurs uniformly at the site). This assumption can be partly justified given the large amount of recharge entering the system. However, lateral transport is also important, for example, as it is the mechanism responsible for moving the contaminant plume away from the S-3 Ponds site, especially in the transition zone. While the limited datasets considered in this study are insufficient to resolve 2D heterogeneity at the site, we expand the 1D model to 2D by assuming that heterogeneity in the hydrological parameters exists in the vertical direction only (i.e., by extrapolating the vertical heterogeneity in the lateral direction). This assumption will be relaxed in subsequent studies as more downgradient hydrogeochemical data become available.

In the 2D model (Figure 8c), the horizontal grid spacing is between 0.5 m and 1 m, and the vertical grid spacing in the fill and Saprolite layers is the same as for the 1D model. As opposed to the 1D model, the transition zone contains multiple grid blocks with 0.25 m vertical spacing. The constant pressure boundary at the lower left side of the transition zone is now represented by multiple grid blocks with a fixed hydrostatic pressure distribution that is shifted by a value determined by inversion.

Heterogeneity in the hydrological parameters is based on the geological layering, with a uniform region in the fill layer, two separate but uniform regions in the Saprolite layer between 2.6 and 6 m and between 6 and 10 m (each representing a zone of potentially different weathering), and a uniform region in the transition zone. Within each of these regions, the

porosity and permeability are uniform and either fixed or estimated by inversion. The parameters of the capillary pressure and relative permeability functions are uniform in the model: two of them (α and n, as defined in *van Genuchten* [1980]) are estimated in Case A (Section 4.3.1).

Two sources of recharge drive the system hydrologically, namely direct infiltration of rainfall, and water from the drainage ditch adjacent to the study site (Figures 4a and 4b). The depth of water in the drainage ditch varies in time, depending on intermittent surface flow from the S-3 Ponds parking lot. This variability is incorporated in the 1D and 2D models (Figures 8b and 8c) through an additional connection that is treated as a time-dependent Dirichlet boundary with either of the following sets of conditions specified: (1) the pressure at the bottom of the ditch that corresponds to the measured water level and 100% water saturation at times when water is present; or (2) atmospheric pressure and 0% water saturation at times when the ditch is dry, making it impermeable to water. The rate at which water enters through the drainage ditch is controlled by the water level in the ditch (a known function of time) and by the permeability of the ditch bed, which is determined in the calibration procedure. It is worth noting that the rate is affected by subsurface moisture conditions, which amounts to a physical coupling between surface water and groundwater. Rainfall-induced infiltration is implemented by specifying a time-dependent flux of water at the surface.

Simulated water level measurements in the saturated zone well (FW120) are obtained by taking the simulated pressures at the top of the screened interval of the well and converting them to hydraulic heads. Simulated water level measurements in the perched zone (SG002) are given by the elevation of the upper-most water-saturated grid block. Simulated nitrate concentration measurements are taken as the concentrations in the grid blocks at the multilevel sampling depths.

The general simulation procedure proceeds as follows for any given set of input hydrogeochemical parameters. In the first step, steady-state conditions are calculated with the pressure in the lower boundary fixed (to a value that is estimated by inversion). The resulting pressure and saturation distributions are then used as initial conditions for the second step of the simulation, which starts on day 98 (April 1). The nitrate concentration is set to zero for the first and second steps of the simulation. The simulation advances as the time-varying rainfall and ditch water level cause transient flow, and water level measurements in the perched and saturated zone wells are simulated on each day (days 98 through 356). At the time of the first geochemical sampling campaign (day 343 or December 9), the third step of the simulation begins. In this step the initial conditions for the nitrate concentration are specified based on values that are also estimated in the inversion (Figure 6c). Naturally, the initial distribution of the nitrate concentration and the recharge-induced flux of water influence the simulated multilevel nitrate concentrations at subsequent geochemical sampling times. The simulated saturation and nitrate concentration distributions at each of the electrical resistivity survey times are used as input to the GM simulations (described in Section 4.2).

4.2. Electrical Resistivity Simulations

For simulating the cross-borehole electrical resistivity measurements collected in the field between wells FW124 and FW125, we are using a 2D grid (shown in Figure 7), with grid discretization in the vertical and horizontal directions ranging from 0.15 m to 0.9 m, and 0.3 m to 1.35 m, respectively.

Coupling between the HM and the GM (see Figure 8d) allows for simulated hydrogeochemical properties to be used as input to the electrical resistivity simulations. In the

cases presented below that consider electrical resistivity data (in Sections 4.3.3 and 4.3.4), output from the 2D hydrogeochemical grid is mapped onto the 2D electrical resistivity grid.

The petrophysical model used to translate the hydrogeochemical properties to the electrical conductivity (inverse of electrical resistivity) distribution needed for the GM has some components that were determined from field data and some that are estimated during the inversion. The electrical conductivity of the pore fluid σ_w [mS/cm] has been empirically related to nitrate concentration C_N [mg/L] at the site using concentration data and co-located electrical conductivity data (from a borehole logging tool), and is given by

$$\sigma_w = aC_N + b, \tag{1}$$

where *a* and *b* are 0.0011 and 3.627, respectively, for the units given in Equation 1; the mean coefficient of determination (R^2) for the fit is 0.81. The influence of temperature on σ_w is not considered since variations in temperature were minor over the time period of the resistivity surveys, and the electrodes used in the study remained below the water table, where temperature varied little with depth.

We consider two models for the electrical conductivity of the variably saturated soil mixture. For the first, we assume the electrical conductivity is adequately described by Archie's law [*Archie*, 1942]:

$$\sigma = \sigma_w \phi^m S_w^n, \tag{2}$$

where ϕ is the porosity, S_w is the water saturation, *m* is the cementation index, and *n* is a constant. At present, we make the relatively common assumption that *n* equals 2 (and is uniform). *Friedman* [2005] summarized studies that investigated the validity of Archie's law for a wide range of water-saturated soils, and observed that the cementation exponent *m* ranges

between 1.2 and 4 for most porous media. He also noted the model is intended for porous media in which surface conduction due to the presence of clays, for example, is minimal.

We also consider the model of *Rhoades et al.* [1976], which contains two fitting parameters (R_1 and R_2) and a term that accounts for surface conduction (σ_s):

$$\sigma = \sigma_w(R_1\theta^2 + R_2\theta) + \sigma_s, \tag{3}$$

where θ is the water content, defined as the product of the porosity and the water saturation. Values of the coefficients of this model for a variety of soil types were reported by *Hamed et al.* [2003].

While the electrical conductivity varies in space as a function of porosity (ϕ) and the time-varying state (S_w and C_N), parameters of the petrophysical model (Equations 1 and 2 or Equations 1 and 3) may be spatially variable as well [*Singha and Moysey*, 2006]. Therefore, we examine the possibility of spatial variability in the cementation index *m* of Equation 2, and the surface conduction σ_s of Equation 3, by estimating their values in various layers as part of the inversion procedure (see Sections 4.3.3 and 4.3.4).

It is worth noting that the petrophysical model is being refined in ongoing laboratory column experiments. While we expect the electrical conductivity of the soil mixture to be mostly controlled by nitrate, additional contributors may turn out to be important (e.g., other fluid constituents, immobile porosity, and surface conduction effects).

4.3. Results

Next we apply the coupled hydrogeophysical modeling approach to several cases with increasing model complexity. In the first case (Case A in Section 4.3.1), an inversion is performed using a 1D representation of the HM, with hydrogeochemical data covering the time

period of days 98 to 362, to obtain estimates of hydrogeochemical parameters that are then fixed or used as initial guesses in most of the subsequent cases. For the second case (Case B in Section 4.3.2), we switch to a 2D representation of the HM that more accurately represents flow and transport at the site, while covering the shorter time period of days 290 to 356. The next set of cases involves inversion of a single electrical resistivity dataset (without performing hydrogeochemical simulations, but using output from the hydrogeochemical simulation of the previous case as input to the electrical resistivity simulations) to estimate parameters of the petrophysical models and examine uncertainty and non-uniqueness issues (Cases C.1 to C.5 in Section 4.3.3). Finally, coupled inversion of the hydrogeochemical datasets with either one or two electrical resistivity datasets is performed (Case D.1 to D.3 in Section 4.3.4). The models and datasets used for each case are listed in Table 1.

The objective function that is minimized during the optimization procedure is formed by contributions from each data type included in a given case. For each data type, the contribution to the objective function is calculated with the least squares criterion, formed by summing the square of the weighted residuals (the difference between the simulated and measured value divided by the standard deviation of the measurement error) for all data points and times. The standard deviation of the measurement error was assumed to be 20 mg/l for the nitrate concentration measurements, and 0.2 m and 0.1 m, respectively, for the water level measurements in the perched-zone and saturated-zone wells. In the contribution of the electrical resistivity data to the objective function, each residual is calculated using the logarithm of the resistance (in units of log Ω) with the standard deviation of measurement error taken to be 10% of the log resistance. The code used in this study automatically orders the electrodes for each

dipole to give positive resistance values, thus allowing for the log transform of the data to be used in the inversion.

For the inversion cases that include all the hydrogeochemical and geophysical data types (Cases D.1 to D.3), the relative contributions to the objective function of the different data types are, approximately, 10% for the water level data, 75% for the geochemical data, and 15% for the electrical resistivity data (for Case D.1); and 9% for the water level data, 66% for the geochemical data, and 25% for the electrical resistivity data (for Cases D.2 and D.3). We leave the testing of alternate formulations of the objective function for future research (e.g., using dipole-dependent measurement error for the electrical resistivity data, and exploring different weighting schemes).

4.3.1. Case A: Inversion of hydrogeochemical data (covering days 102 to 362) with 1D HM

In this case inversion is performed using a 1D HM with hydrogeochemical data corresponding to a relatively long time period of 260 days, during which numerous wetting and drying cycles occurred (see Figure 4). As listed in Table 2, the parameters considered unknown are four permeability values (for the Saprolite layers, the transition zone, and the ditch); one porosity value (for the combined Saprolite layers); two parameters of the capillary pressure and relative permeability functions (parameters α and n of the *van Genuchten* [1980] functions); eight concentrations that define the initialization profile at day 343 in the Saprolite layer (since the transition zone is not modeled in detail in the 1D model; see Figure 6b); and the constant pressure value at the lower boundary, for a total of 16 unknown parameters. The hydrogeochemical data used in the inversion are the daily water level data collected between

days 102 and 362 from the perched and saturated-zone wells, and data from three geochemical sampling depths at six survey times (days 343, 344, 346, 349, 351, and 356).

Given the considerations on the limited amount of data and resulting non-uniqueness, certain parameters could not be estimated independently and were instead set to reasonable values (e.g., the porosity of the fill layer and the permeability of the transition zone).

The estimated values and uncertainties for all of the parameters except the initial concentrations are given in Table 2; the estimated initial concentration profile is shown in Figure 6c. The permeability in the fill layer is estimated to be on the order of 5E-11 m^2, while that of the upper and lower portions of the Saprolite, respectively, are 3 orders of magnitude lower (4E-14 m^2) and 2 orders of magnitude lower (1.6E-13 m^2). The porosity in the combined Saprolite layers is estimated to be 0.36.

Figure 9 shows the fit between the measured and simulated water level data (Figures 9a and 9b) and the nitrate concentration data (Figure 9c). The water level behavior in both wells is captured reasonably well, though the simulated water level in FW117 rises faster after day 300 than the measured response. The trends of the nitrate concentrations at each depth are also reproduced.

Some of the observed differences between the simulated and measured data are likely due to inherent model error, such as 2D or 3D effects or effects occurring over long time scales that are not adequately accounted for. Regardless, it is promising that the complex water level and nitrate concentration behavior in the upper part of the model can be explained with a relatively simple 1D model. The corresponding parameter estimates can now be transferred to the 2D model and fixed or used as initial guesses. The parameters α and n of the capillary pressure function are fixed in the remaining cases to the values estimated in this section.

4.3.2. Case B: Inversion of hydrogeochemical data (covering days 290 to 356) with 2D HM

To better represent flow and transport at the site, we switch to a more accurate 2D representation of the HM and perform inversions with additional hydrogeochemical data (collected at three depths in the transition zone). Because of the increased computational demands of the 2D model, we focus on data collected during the shorter time period of days 290 to 356. In addition to estimating most of the parameters considered in the previous case, we also estimate the porosity in the transition zone, as well as four more parameters of the initial nitrate concentration profile (corresponding to depths in the transition zone). The parameters α and n of the capillary pressure function are fixed to the values estimated in Case A.

The measured and simulated water level and nitrate concentration data are shown in Figure 10. Relative to Figure 9, this figure differs in that the measured and simulated nitrate concentrations for the transition zone (at depths of 11.5, 13.2 and 15.2 m) are included, and the shorter time period is focused on the prolonged wetting phase beginning around day 300.

The estimated values and uncertainties of the 19 parameters for this case are given in Table 2. It is interesting to note that while the values remain similar to those for Case A, the uncertainty of the estimated hydrological parameters is increased relative to Case A. This is probably a result of the shorter time period considered, which mainly experiences a prolonged wetting (or wet) phase. The wetting and drying cycles that occur in the time period for Case A lead to increased sensitivity of the water level data to the hydrological parameters. The increased uncertainty may also be related to the wider range of phenomena that can occur in the 2D model as water enters the model from the ditch, spreads laterally, and causes intermittent water ponding.

As discussed previously (in Section 4.1), we initialized the nitrate transport component of the simulation by specifying the vertical profile of the concentration at day 343 based on parameters that are estimated in the inversion. This was necessary because of the high sensitivity of the response to the assumed shape of the initial profile. To highlight this issue, the simulated response of the nitrate measurements are shown in Figure 11 as a function of time for three different initial profiles, with all other parameters of the HM remaining unchanged. The first two profiles were obtained by linear and nearest-neighbor interpolation (see Figure 6b) of the multilevel geochemistry data collected on day 343, and the third was estimated by inversion (see Case B in Figure 6c). Since both of the profiles obtained by interpolation honor the geochemistry data at the sampling locations (shown with symbols in Figure 6b), one might assume that either would serve as adequate initial conditions for the inverse modeling procedure. However, as is evident in Figure 11, the response varies significantly depending on the initial profile, and not all of the profiles allow for the observed response to be adequately reproduced. The responses at 8, 13, and 15.2 m depth are seen to be generally similar for all initial profiles: the concentrations decrease with time. The interesting thing to note is in the responses for the interpolated profiles at 10 and 11.5 m, which exhibit the trend of continuously increasing concentration with time. In contrast, using the profile that was estimated by inversion, the shape of the response is more similar to that of the measured response, namely, showing a decrease in concentration after an initial increase. This is explained by considering the results of the inversion, which predict that there is a zone of decreased concentration at around 8.5 to 9 m depth (Figure 6c). Such a zone of decreased concentration was not captured by the limited multilevel geochemistry samples, but it appears to be important for modeling the response of nitrate to fresh water dilution. These results

highlight the importance of accurately modeling the initial conditions, as well as the contaminant source term, in order to make accurate transport predictions.

The simulated water saturation distribution at day 345 is shown in Figure 12, as are the nitrate concentration distributions at days 345 and 354, corresponding to the electrical resistivity surveys discussed below (in Sections 4.3.3 and 4.3.4). The water table remains high during this short time period. Due to the large contrast between the fill layer and the underlying Saprolite layer, the water originating from the ditch moves laterally much faster than vertically, spreading out over the model domain before migrating vertically. An overall displacement of the low concentration front is observed to travel downward and toward the outflow region in the transition zone.

4.3.3. Cases C.1 to C.5: Inversion of single electrical resistivity survey using output from 2D HM

The cases in this section involve the inversion of a single electrical resistivity dataset from the survey conducted on day 343. No hydrogeochemical data are included in the objective function, and no hydrogeochemical simulations are performed. However, output from the hydrogeochemical simulation of Case B (Section 4.3.2) at day 343 is used as fixed input to the electrical resistivity simulations. Note that due to insensitivity of the electrical resistivity data to the properties of the fill layer, which only extends 2.6 m in depth, the petrophysical parameters of the fill layer are assigned the same values as those of the upper Saprolite zone, some of which are estimated by inversion.

First we consider Archie's law (Equation 2) to describe the electrical conductivity of the soil/rock mixture (the fluid conductivity is given as a function of the nitrate concentration by Equation 1). Several inversion cases are considered to examine possible heterogeneity in

parameter *m*: one case (Case C.1) where it is assumed to be spatially uniform, and three cases (Cases C.2 to C.4) where multiple zones or regions, each corresponding to a distinct value of *m*, are assumed to exist. For the case in which *m* is modeled as homogeneous for the entire model, its estimated value is 1.01, which is below the expected range of 1.2 to 4 (see Section 4.2). In Case C.2, two regions with distinct values of *m* are assumed to exist: for the region containing the Saprolite it is estimated to be 1.72; and for the region containing the transition zone it is estimated to be 0.97. In the next two cases, three regions with distinct values of *m* are assumed to exist: two regions are formed by the upper and lower halves of the Saprolite while the third is formed by the transition zone in Case C.3, and two regions are formed by the upper and lower halves of the transition zone while the third is formed by the Saprolite in Case C.4. In all of the Cases C.2 to C.4, the *m* values are estimated to be consistently higher in the Saprolite, ranging between 1.72 and 1.9, than in the transition zone, ranging between 0.94 and 0.97. The estimated values and the uncertainty in the estimates are reported in Table 3. Note that the observed low values of m may be due to surface conduction or immobile porosity, which are not accounted for.

The sensitivity of the objective function to the parameters considered in Cases C.1 to C.4 is depicted in Figure 13. Recall that for these cases, the only contribution to the objective function comes from a single electrical resistivity data set collected on day 343. For each curve, the specified parameter is varied and the objective function is calculated, while any remaining parameters are fixed at the values that were estimated by inversion. Since the shape of each curve depends on the values of the other parameters, these figures show approximate relationships and are mainly intended to help understand potential issues of non-uniqueness and parameter identifiability.

For Case C.1, the minimum of the objective function is clearly defined (Figure 13a), but its value of 539 is higher than for the remaining cases (see Table 3), revealing that it is likely not appropriate to assume *m* is spatially uniform at this site. Note the vertical scale in Figure 13a is different from that in Figures 13b-d. Performing the inversion with the assumption that heterogeneity in *m* can be described using two regions (Case C.2) results in an overall decrease in the minimum value of the objective function to 421 (20% lower than the previous case), and uniquely determined values of *m* for both regions. When adding a second region for which *m* is to be estimated in the Saprolite layer (Case C.3), making three regions in total, inversion results in a minimum objective function value of 415, though the objective function is relatively insensitive to *m* in the upper-most layer (Figure 13b). When instead adding a second region for which *m* is to be estimated in the transition zone (Case C.4), the minimum value of the objective function is 417, and each value is uniquely determined. Given that the inversions for the three-layer cases (Cases C.3 and C.4) result in minimum objective function values that are only marginally lower than for the two-layer case (Case C.2), and given that the two layers estimated in the transition zone in Case C.4 appear to have nearly the same value (0.94 and 0.97), we conclude that heterogeneity in *m* can be described sufficiently using the two-region parameterization of Case C.2.

We also consider the Rhoades model (Equation 3) for modeling the electrical conductivity of the soil/rock mixture (Case C.5). The parameters R_1 and R_2 are assumed to be spatially uniform and are estimated by inversion, while the log of the surface conduction σ_s is estimated for two regions: one that contains the Saprolite (and fill layer), and one that contains the transition zone. The estimated values of the log surface conduction term correspond to actual values for σ_s of 0.017 and 0.066 S/m, respectively (see Table 3), indicating that surface conduction a) may play a

significant role at the site, and b) may be around four times higher in the transition zone than in the Saprolite. The shape of the objective function in the vicinity of the estimated parameter values is shown in Figure 14. The objective function is relatively flat for low values of σ_s (i.e., for log (σ_s S/m]) values less than approximately -1.6). With a minimum value of the objective function equal to 428 (see Table 3), this petrophysical model allows for a fit to the electrical resistivity data that is similar to that obtained in Cases C.1-C.4, but it requires four parameters instead of, for example, only two parameters needed for Case C.2.

The measured and simulated electrical resistivity data for two representative petrophysical model cases, Cases C.2 (Figure 15a) and C.5 (Figure 15b), show a nearly identical fit. The average error is nearly the same for each: for Case C.2, the median and standard deviation of the residuals of the log resistance data are 0.004 and 0.25 [log Ω], respectively; and for Case C.5, the corresponding values are -0.006 and 0.25 [log Ω]. Each subplot shows the dipole measurements for a current dipole at a single depth. The misfit is largest for the measurements at the deepest current dipoles (CD 1 to CD 7).

4.3.4. Cases D.1 to D.3: Coupled inversion of hydrogeochemical data (covering days 290 to 356) and electrical resistivity data with 2D HM

In the final three cases, we perform coupled inversion of all the hydrogeochemical data considered in Case B and one electrical resistivity survey dataset collected on days 343 (Case D.1) or the two electrical resistivity survey datasets collected on days 343 and 354 (Cases D.2 and D.3), as described in Table 1. The estimated parameters include the hydrogeochemical parameters that were estimated in Case B (Table 2) and the two parameters of the petrophysical model (Archie's model) that were estimated in Case C.2 (Table 3).

For Case D.1, the initial parameter guesses for the hydrogeochemical parameters were taken as the estimated values from Case B, and those for the petrophysical parameters were taken as the estimated values from Case C.2. Many of the parameter estimates resulting from the coupled inversion are similar to the initial guesses (i.e., the values obtained in Case B and Case C.2), suggesting that the initial guesses were already close to the true values. However, the standard deviations of the hydrological parameter estimates are lower in this case. In addition, the petrophysical parameter *m* for the Saprolite and fill layers decreased from 1.72 to 1.62, and that for the transition zone decreased from 0.97 to 0.88.

For Case D.2, two electrical resistivity datasets are included, along with the hydrogeochemical datasets that were included in Case D.1. Including the additional electrical resistivity dataset has the effect of increasing the amount of weight assigned to the electrical resistivity data (from 15% to 25%, as mentioned above). However, the parameter estimates remain mostly unchanged (within the standard deviation) from the previous case.

In Case D.3, we examine the sensitivity of the results to the initial conditions, and the overall stability of the inversion. The setup for the inversion is the same as for Case D.2 except that most of the initial guesses are intentionally set at values that are significantly different from those estimated in Sections 4.3.2 and 4.3.3. The initial values of parameter *m* for the Saprolite and the transition zone are now 1.3 (instead of 1.72 and 0.97, respectively). The initial guesses for the log permeability of the fill, upper Saprolite, lower Saprolite, and the ditch are -10.5, -13, -12, -10.5, respectively (instead of -9.8, -13.5, -12.6, -9.9). The initial porosity values in the Saprolite and in the transition zone are 0.25 and 0.2, respectively (instead of 0.33 and 0.12). The remaining parameters have initial guesses that are unchanged relative to Case B. Whereas the initial value of the objective function for Case D.2 was 3809, the value for this case is five times higher

(19054). However, the inversion for this case resulted in the minimum value of the objective function of 3606, which is only 2% higher than the minimum achieved in Case D.2. The parameter estimates are mostly similar to the previous case for the hydrogeochemical parameters, though the estimated value of constant pressure at the outflow boundary is increased. In addition, the porosity estimate in the Saprolite layers increased from 0.362 to 0.382, and the petrophysical parameter m for the Saprolite layers increased from 1.68 to 1.75. Overall, it appears that the inversion is stable and not overly sensitive to initial conditions.

The measured electrical resistivity data and the values simulated with the parameters obtained in the inversion for Case D.2 are shown in Figure 16a. Note that while the fit between measured and simulated data is good, the variation in time from day 343 to 354 is relatively small, implying potentially low sensitivity of the data to the changing nitrate concentrations. The temporal variations would of course be larger if coincident geophysical-hydrological-geochemical datasets were collected at additional times during which different hydrological conditions prevailed (e.g., earlier in the wetting phase or during a drying phase, rather than only the closely spaced surveys during the sustained wet phase).

The coupled model that was developed in this section (specifically, using the parameters estimated in Case D.2) can be used to examine the sensitivity of different types of datasets for understanding the spatiotemporal variations in subsurface processes. For example, the potential gain in sensitivity from including an electrical resistivity dataset at a later time is depicted in Figure 16b. The simulated time-lapse electrical resistivity data are shown for days 345 and 365, a time lapse of 20 days (as opposed to the time lapse of 9 days between the actual surveys that were conducted on days 345 and 354). Overall, the time-varying differences between measurements are larger, indicating better sensitivity due to the fact that the nitrate concentration

and thus the electrical properties are predicted to change more by day 365 than they had by day 354. Further increased sensitivity would likely be achieved if some electrical resistivity (and geochemical) datasets were collected before the onset of the wetting phase, likely leading to improved parameter estimates.

5. Summary and Conclusions

In this work we develop a coupled hydrogeochemical-geophysical model that honors a variety of data types collected in a field measurement campaign at the S3-Ponds experimental site at the Oak Ridge IFRC site. Our approach allows for the simulation of hydrogeochemical processes, such as the dilution of subsurface nitrate contamination resulting from high recharge events, and the corresponding geophysical responses.

Coupled inversion of the time-varying water level data, nitrate concentration data and electrical resistivity data provided estimates of various hydrogeochemical parameters, such as permeability and porosity, and various petrophysical parameters for a number of geological layers in the model. The inverse modeling was performed in an incremental fashion, adding data sets and increasing model complexity with each step. Inversion of only the hydrogeochemical data was first performed using a computationally efficient, simplified 1D representation of the HM over a long time series of data, and was then followed by application of a 2D representation of the HM that was more accurate but covered a shorter time period. The low permeability Saprolite layer underlying a high permeability fill zone was seen to cause intermittent water ponding, which is captured in the model, as evidenced by reproduction of the water level time series in a perched-zone well and a saturated zone well. In addition, the modeled response of the nitrate measurements was also reproduced. We found that the results were highly sensitive to the

nitrate concentration profile used to initialize the simulations, necessitating its concurrent estimation in the inversion procedure.

Two different petrophysical relationships for the electrical conductivity of the soil/rock mixture were considered: Archie's law and Rhoades model. (The fluid conductivity was fixed based on a relationship between the measured nitrate concentrations and electrical conductivity logging data.) We observed that a) spatial variability in the petrophysical model must be accounted for, b) a two-layer model appears to be sufficient for describing heterogeneity of the petrophysical model at the site, c) the parameter *m* of Archie's model was lower than expected in one region (the transition zone), and d) based on application of Rhoades model, surface conduction may be an important consideration for the subsurface materials at the site (and may explain the anomalously low value of *m* estimated for Archie's model). The low value of m could also be due to immobile porosity which is not taken into account. We also examined non-uniqueness and uncertainty in the petrophysical parameters by examining the shape of the objective function for different cases, which helped identify an acceptable parameterization of spatial heterogeneity. The validity of the petrophysical functions inferred in this study will be examined using the results from laboratory column experiments that are underway.

The coupled inversion procedure yielded hydrogeochemical and petrophysical parameter estimates that were similar regardless of whether one or two electrical resistivity datasets were included, and the inversion was stable when initial conditions were set intentionally far from the values estimated in previous steps.

Overall, sensitivity of the electrical resistivity data to temporal changes in the nitrate concentration was found to be somewhat low, but this may simply be a reflection of the limited

time period during which the electrical resistivity and geochemical surveys were conducted (during a sustained wetting phase).

While the 2D HM used in this study accounts for flow from a drainage ditch and from precipitation-induced infiltration, we assume the model parameters are continuous in the lateral direction (though heterogeneous in the vertical direction). To resolve heterogeneity in the horizontal direction, a more comprehensive model will be developed for the site that incorporates flowmeter and slug test data and spatially distributed geochemistry data (as opposed to only using geochemistry data from a single well) as they become available. In addition, the contaminant source should be accurately represented, and a dual-domain implementation of flow and transport at the site considered.

This study illustrates the potential for the coupled modeling framework to be used as a tool for integrating multiple types of data at the local scale (such as borehole and cross-borehole datasets) in order to examine the relationships between recharge, soil characteristics, initial contaminant concentration, and transport processes at a contaminated site. Further studies using the coupled modeling framework are planned that consider geophysical and geochemical datasets collected during a wider range of conditions, for example, during wetting, wet, and drying phases. It is expected that applying the inverse modeling procedure under more varied and dynamic conditions will increase parameter sensitivity and allow improved understanding of the system processes. Subsequent studies will incorporate sparser but more spatially extensive datasets (e.g., surface-based electrical resistivity data) for monitoring recharge-related hydrogeochemical variations over larger scales.

Acknowledgements

This work was supported by the U.S. Department of Energy, Contract No. DE-AC02-05CH11231 and by the Environmental Remediation Program of the U.S. DOE Office of Biological and Environmental Research as part of the Oak Ridge National Laboratory IFRC Study. The authors would like to thank Andreas Kemna (University of Bonn) for the use of the code CRMOD, Marcella Mueller (ORNL) for assistance with the hydrogeochemical data, and Jack Parker (ORNL) for input on the site conceptual model, and Akiko Yoshikawa for additional support. We are grateful to Lee Slater, Andrew Binley, Tim Johnson, and an anonymous reviewer for constructive feedback and excellent suggestions for improving the manuscript.

References

Archie, G. E. (1942), The electrical resistivity log as an aid in determining some reservoir characteristics, *Trans. Amer. Inst. Mineral. Mat.*, *146*, 54–62.

Binley, A., G. Cassiani, R. Middleton, and P. Winship (2002), Vadose zone flow model parameterization using cross-borehole radar and resistivity imaging, *J. of Hydrol.*, *267*, 147-159.

Cassiani, G. and A. Binley (2005), Modeling unsaturated flow in a layered formation under quasi-steady state conditions using geophysical data constraints, *Adv. Water Resour.*, 28(5), 467-477.

Chen, J., S. Hubbard, J. Peterson, K. Williams, M. Fienen, P. Jardine, and D. Watson (2006), Development of a joint hydrogeophysical inversion approach and application to a contaminated fractured aquifer, *Water Resour. Res.*, 42(6).

Chen, J., S. S. Hubbard, D. P. Gaines, V. Korneev, G. S. Baker, and D. B. Watson (2010), Stochastic Estimation of Aquifer Geometry Using Seismic Refraction Data with Borehole Depth Constraints, *Water Resour. Res.*, doi:10.1029/2009WR008715, in press.

Daily, W. D., and A. L. Ramirez (2000), Electrical imaging of engineered hydraulic barriers, *Geophysics*, *65*(1), 83–94.

Daily, W. D., A. L. Ramirez, D. J. LaBrecque, and J. Nitao (1992), Electrical resistivity tomography of vadose water movement, *Water Resour. Res.*, *28*, 1429–1442.

Daily, W.D., and A.L. Ramirez, Electrical resistance tomography during in-situ trichloroethylene remediation at the Savannah River site (1995), *J. Appl. Geophys.*, *33*, 1429–1442.

Day-Lewis, F. D., and J. W. Jr., Lane (2004), Assessing the resolution-dependent utility of tomograms for geostatistics, *Geophys. Res. Lett.*, *31*(7), L07503, doi:10.1029/2004GL019617.

Day-Lewis F. D., K. Singha (2008), Geoelectrical inference of mass transfer parameters using temporal moments, Water Resour. Res., 44, W05201, doi:10.1029/2007WR006750.

Deiana, R., G. Cassiani, A. Villa, A. Bagliani, and V. Bruno (2008), Calibration of a vadose zone model using water injection monitored by GPR and electrical resistance tomography, *Vadose Zone J.*, *7*, 215–226.

Farmani, M.B., H. Keers, and N.O. Kitterød (2008), Time lapse GPR tomography of unsaturated water flow in an ice-contact delta, *Vadose Zone J.*, *7*, 272–283.

Ferré, T. P. A., A. C. Hinnell and J. B. Blainey (2006), Inferring hydraulic properties using surface-based electrical resistivity during infiltration, *The Leading Edge*, *25*(6), 720–723, doi: 10.1190/1.2210055.

Finsterle, S. (1999), iTOUGH2 User's Guide, Report LBNL-40040, Lawrence Berkeley National Laboratory, Berkeley, CA.

Finsterle, S. (2004), Multiphase inverse modeling: Review and iTOUGH2 applications, *Vadose Zone J.*, *3*, 747–762.

Finsterle, S., and M.B. Kowalsky (2008), Joint hydrological-geophysical inversion for soil structure identification, *Vadose Zone J.*, *7*, 287–293, doi:10.2136/vzj2006.0078.

French, H.K., C. Hardbattle, A. Binley, P. Winship, L. Jakobsen (2002), Monitoring snowmelt induced unsaturated flow and transport using electrical resistance tomography, *J. Hydrol.*, 267, 273–284.

Friedman, S. P. (2005), Soil properties influencing apparent electrical conductivity: a review, *Computers and Electronics in Agriculture*, 46, 45-70.

Gaines, D.P., G.S. Baker, S.S. Hubbard, D. Watson and P. Jardine (2009), Application of Surface Time-Lapse Seismic Refraction Tomography (TLSRT) to Quantifying Changes in Saturation Within the Vadose Zone, Eos. Trans., AGU, 90(22), Jt. Assem. Suppl., Abstract H13D-05.

Hamed, Y., M. Persson, and R. Berndtsson (2003), Soil Solution Electrical Conductivity Measurements Using Different Dielectric Techniques, *Soil Science Society of America Journal*, *67*, 1071-1078.

Hinnell, A. C., T. P. A. Ferré, J. A. Vrugt, J. A. Huisman, S. Moysey, J. Rings, and M. B. Kowalsky (2010), Improved extraction of hydrologic information from geophysical data through coupled hydrogeophysical inversion, *Water Resour. Res.*, 46, W00D40, doi:10.1029/2008WR007060.

Jadoon K. Z., E. Slob, M. Vanclooster, H. Vereecken, S. Lambot (2008), Uniqueness and stability analysis of hydrogeophysical inversion for time-lapse ground-penetrating radar estimates of shallow soil hydraulic properties, *Water Resour. Res.*, *44*, W09421, doi:10.1029/2007WR006639.

Johnson, T. C., R. J. Versteeg, H. Huang, P. Routh (2009), Data-domain correlation approach for joint hydrogeologic inversion of time-lapse hydrogeologic and geophysical data, *Geophysics*, 74(6), F127–F140, doi: 10.1190/1.3237087.

Kemna, A. (2000), Tomographic inversion of complex resistivity—Theory and application, Ph.D. thesis, Bochum University.

Kemna, A., J. Vanderborght, B. Kulessa and H. Vereecken (2002), Imaging and characterization of subsurface solute transport using electrical resistivity tomography (ERT) and equivalent transport models, *J. of Hydrology*, *267*(3-4), 125–146.

Kowalsky, M.B., J. Birkholzer, J. Peterson, S. Finsterle, S. Mukhopadhyay, and Y. Tsang (2008), Sensitivity analysis for joint inversion of GPR and thermal-hydrological data from a large-scale underground heater test, *Nuclear Technology*, *164*(2), 169–179.

Kowalsky, M.B., S. Finsterle, J. Peterson, S. Hubbard, Y. Rubin, E. Majer, A. Ward and G. Gee (2005), Estimation of field-scale soil hydraulic and dielectric parameters through joint inversion of GPR and hydrological data, *Water Resour. Res.*, *41*(11), W11425, doi:10.1029/2005WR004237.

Kowalsky, M.B., S. Finsterle, and Y. Rubin (2004), Estimating flow parameter distributions using ground-penetrating radar and hydrological measurements during transient flow in the vadose zone, *Adv. in Water Resour.*, *27*(6), 583–599.

Kowalsky, M.B., S. Nakagawa, and G.J. Moridis (2010), Feasibility of monitoring gas hydrate production with time-lapse vertical seismic profiling, *SPE J.*, 15(3), 634-645, doi: 10.2118/132508-PA.

Lambot, S., E. C. Slob, M. Vanclooster, and H. Vereecken (2006), Closed loop GPR data inversion for soil hydraulic and electric property determination, *Geophys. Res. Lett., 33*, L21405, doi:10.1029/2006GL027906.

Lehikoinen, A., S. Finsterle, A. Voutilainen, M.B. Kowalsky, and J.P. Kaipio, Dynamical inversion of geophysical ERT data: state estimation in the vadose zone (2009b), *Inverse Problems in Sci. and Eng.*, 17(6), 715-736, doi: 10.1080/17415970802475951.

Lehikoinen, A., J.M.J. Huttunen, S. Finsterle, M.B. Kowalsky, and J.P. Kaipio (2010), Dynamic inversion for hydrological process monitoring under model uncertainties, *Water Resour. Res.*, 46, W04513, doi:10.1029/2009WR008470.

Looms, M.C., K.H. Jensen, A. Binley, and L. Nielsen (2006), Monitoring unsaturated flow and transport using cross-borehole geophysical, *Vadose Zone J.*, *7*, 227–237.

Looms, M.C., A. Binley, K.H. Jensen, L. Nielsen, and T.M. Hansen (2008), Identifying unsaturated hydraulic parameters using an integrated data fusion approach on cross-borehole geophysical data, *Vadose Zone J.*, *7*, 238–248.

Park, S. (1998), Fluid migration in the vadose zone from 3-D inversion of resistivity monitoring data, *Geophysics*, 63(41), doi:10.1190/1.1444326.

Peterson, J. E., B. N. P. Paulsson, and T. V. McEvilly (1985), Applications of algebraic reconstruction techniques to crosshole seismic data, *Geophysics*, *50*, 1566–1580.

Pollock, D., and O. A. Cirpka (2008), Temporal moments in geoelectrical monitoring of salt tracer experiments, *Water Resour. Res.*, *44*, W12416, doi:10.1029/2008WR007014.

Pruess, K., C. Oldenburg, G. Moridis (1999), TOUGH2 User's Guide, Version 2.0, Report LBNL-43134, Lawrence Berkeley National Laboratory, Berkeley, CA.

Ramirez, A., W. Daily, A. Binley, D. LaBrecque, D. Roelant (1996), Detection of leaks in underground storage tanks using electrical resistance methods, *J. Environ. Eng. Geophys.*, *1*, 189–203.

Ramirez, A., W. Daily, D. LaBrecque, E. Owen, and D. Chesnut (1993), Monitoring an underground steam injection process using electrical resistance tomography, *Water Resour. Res.*, *29*, 73–87.

Rhoades, J.D., P.A.C. Ratts, and R.J. Prather (1976), Effects of liquid-phase electrical conductivity, water content, and surface conductivity on bulk soil electrical conductivity, *Soil Sci. Soc. Am. J.*, *40*, 651–655.

Rucker, D.F., and T.P.A. Ferré (2004), Parameter estimation for soil hydraulic properties using zero-offset borehole radar: Analytical method, *Soil Science Society of America Journal*, *68*, 1560–1567.

Singha K., S. M. Gorelick (2005), Saline tracer visualized with three-dimensional electrical resistivity tomography: Field-scale spatial moment analysis, *Water Resour. Res.*, 41, W05023, doi:10.1029/2004WR003460.

Singha, K. and Moysey, S. (2006), Accounting for spatially variable resolution in electrical resistivity tomography through field-scale rock physics relations, *Geophysics*, *71*(4), A25–A28, dio:10.1190/1.2209753.

Slater, L., A.M. Binley, W. Daily, and R. Johnson (2000), Cross-hole electrical imaging of a controlled saline tracer injection, *J. of Applied Geophysics*, *44*, 85–102.

van de Hoven, S.J., D.K. Solomon, and G.R. Moline (2005), Natural spatial and temporal variations in groundwater chemistry in fractured, sedimentary rocks: scale and implications for solute transport, *Applied Geochemistry*, *20*, 861–873.

van Genuchten, M. T. (1980), A closed-form equation for predicting the hydraulic conductivity of unsaturated soils, *Soil Science Society of America Journal*, *44*, 892–898.

Yeh T.-C. J., S. Liu, R. J. Glass, K. Baker, J. R. Brainard, D. L. Alumbaugh, and D. LaBrecque (2002), A geostatistically based inverse model for electrical resistivity surveys and its applications to vadose zone hydrology, *Water Resour. Res.*, *38*(12), 1278, doi:10.1029/2001WR001204.

Zhou, Q. Y., J. Shimada, and A. Sato (2001), Three dimensional spatial and temporal monitoring of soil water content using electrical resistivity tomography, *Water Resour. Res.*, *37*, 273–285.

Table 1. Summary of inversion cases and datasets.

Description	**Case A**	**Case B**	**Cases C.1-C.5**	**Cases D.1**	**Cases D.2-D.3**
Related section in text	4.3.1	4.3.2	4.3.3	4.3.4	4.3.4
Simulation period for HM	days 102–362	days 290–356	–	days 290–356	days 290–356
Models					
Hydrogeochemical	1D	2D	–	2D	2D
Electrical resistivity	– [a]	–	2D	2D	2D
Datasets					
Nitrate conc. in well FW120 (at 5.5, 8, and 10 m)	Six measurements during days 343–356	Six measurements during days 343–356	–	Six measurements during days 343–356	Six measurements during days 343–356
Nitrate conc. in well FW120 (at 11.5, 13.2, and 15.2 m)	–	Six measurements during days 343–356	–	Six measurements during days 343–356	Six measurements during days 343–356
Water level in well SG002	252 measurements during days 102–362	58 measurements during days 290–356	–	58 measurements during days 290–356	58 measurements during days 290–356
Water level in well FW117	261 measurements during days 102–362	67 measurements during days 290–356	–	67 measurements during days 290–356	67 measurements during days 290–356
Electrical resistivity	–	–	One measurement survey on Day 345	One measurement survey on day 345	Two measurement surveys on days 345 and 354

[a]The dash symbol "–" indicates that category is not applicable.

Table 2. Parameter values of hydrogeochemical model for different inversion cases considered in Section 4.3.

Parameters	**Case A**	**Case B**	**Cases C.1-C.5**	**Case D.1**	**Case D.2**	**Case D.3**
Hydrological						
log (k_{ditch} [m^2])	-9.95 (±0.02)[a]	-9.91 (±0.05)	*Fixed*[b]	-9.93 (±0.02)	-9.92 (±0.02)	-9.86 (±0.02)
log (k_{fill} [m^2])	-10.29 (±0.02)	-9.8 (±0.5)	*fixed*	-9.53 (±0.09)	-9.49 (±0.2)	-10.03 (±0.08)
log ($k_{upper\ Sap.}$ [m^2])	-13.39 (±0.02)	-13.47 (±0.04)	*fixed*	-13.43 (±0.01)	-13.42 (±0.01)	-13.43 (±0.01)
log ($k_{lower\ Sap.}$ [m^2])	-12.79 (±0.01)	-12.6 (±0.2)	*fixed*	-12.73 (±0.05)	-12.71 (±0.05)	-12.33 (±0.09)
log ($k_{tran.}$ [m^2])	*fixed (-10)*	*fixed*	*fixed*	*fixed*	*fixed*	*fixed*
ϕ_{fill}	*fixed (0.15)*	*fixed*	*fixed*	*fixed*	*fixed*	*fixed*
$\phi_{upper\ and\ lower\ Sap.}$	0.36 (±0.02)	0.33 (±0.05)	*fixed*	0.351 (±0.01)	0.362 (±0.004)	0.382 (±0.004)
$\phi_{tran.}$	*fixed (0.15)*	0.12 (±0.01)	*fixed*	0.125 (±0.003)	0.126 (±0.003)	0.134 (±0.002)
log (α [Pa^{-1}])[c]	2.96 (±0.01)	*fixed*	*fixed*	*fixed*	*fixed*	*fixed*
n[d]	3.2 (±0.2)	*fixed*	*fixed*	*fixed*	*fixed*	*fixed*
$dP_{outflow}$ [kPa]	4.3 (±0.2)	3.9 (±1.0)	*fixed*	3.3 (±0.46)	3.3 (±0.42)	5.15 (±0.34)
Initial conc. (Fig. 6c)						
log $C_{i=1,8}$ *(d < 10 m)*	*estimated*[d]	*estimated*	*fixed*	*estimated*	*estimated*	*estimated*
log $C_{i=9,12}$ *(d > 10 m)*	–[e]	*estimated*	*fixed*	*estimated*	*estimated*	*estimated*
Objective function						
Initial value	9037	3138	See Table 3	3177	3809	19054
Final value	2503	2661	See Table 3	3098	3528	3606

[a]Standard deviations are given for the parameter estimates after the symbol "±".
[b]*Fixed* indicates the parameter is set to the value in parentheses (if given) or else to the value for the Case (column) to the left.
[c]Parameters of the capillary pressure function of *van Genuchten* [1988].
[d]Estimated concentration values are shown in Figure 6.
[e]The dash symbol "–" indicates that the category is not applicable.

Table 3. Parameter values of electrical resistivity model for different inversion cases considered in Section 4.3.

Parameters	**Cases A-B**	**Case C.1**	**Case C.2**	**Case C.3**	**Case C.4**	**Case C.5**	**Case D.1**	**Case D.2**	**Case D.3**
Model									
σ (bedrock) [S m^{-1}]	–[a]	*fixed*[b] *(1E-4)*	*fixed*	*fixed*	*fixed*	*fixed*	*fixed*	*fixed*	*fixed*
Fluid electrical conductivity σ_w (Eq. 1)									
A	–	*fixed (0.0011)*	*fixed*	*fixed*	*fixed*	*fixed*	*fixed*	*fixed*	*fixed*
B	–	*fixed (3.627)*	*fixed*	*fixed*	*fixed*	*fixed*	*fixed*	*fixed*	*fixed*
Archie's model (Eq. 2)									
n	–	*fixed (2)*	*fixed*	*fixed*	*fixed*	–	*fixed*	*fixed*	*fixed*
m_1 (fill)	–	1.01 (±0.01)[c]	1.72 (±0.01)	1.90 (±0.03)	1.83 (±0.01)	–	1.62 (±0.04)	1.68 (±0.03)	1.75 (±0.02)
m_2 (upper Sap.)	–					–			
m_3 (lower Sap.)	–			1.72 (±0.01)		–			
m_4 (upper tran.)			0.97 (±0.01)	0.97 (±0.01)	0.97 (±0.01)	–	0.88 (±0.01)	0.85 (±0.01)	0.88 (±0.01)
m_5 (lower tran.)					0.94 (±0.01)	–			
Rhoades model (Eq. 3)									
log (σ_s [S/m]) (fill and Sap.)	–	–	–	–	–	-1.77 (±0.04)	–	–	–
log (σ_s [S/m]) (tran.)	–	–	–	–	–	-1.18 (±0.01)	–	–	–
R_1 (all layers)	–	–	–	–	–	-0.31 (±0.03)	–	–	–
R_2 (all layers)	–	–	–	–	–	0.47 (±0.01)	–	–	–
Objective function									
Initial value	See Table 2	678	678	626	626	619	3177	3809	19054
Final value	See Table 2	539	421	415	417	428	3098	3528	3606

[a]The dash symbol "–" indicates that the category is not applicable.
[b]*Fixed* indicates the parameter is set to the value in parentheses (if given) or else to the value for the Case (column) to the left.
[c]Standard deviations are given for the parameter estimates after the symbol "±".

Figure Captions

Figure 1. Depiction of the coupled hydrogeophysical modeling approach.

Figure 2. Oak Ridge Integrated Field Research Challenge (IFRC) site: (a) location in eastern Tennessee, (b) unlined surface trenches (the S-3 Ponds) that received approximately 2.5 million gallons per year of waste containing acidic nitrate and uranium, among other contaminants, from 1951 to 1983, (c) parking lot covering S-3 Ponds after they were capped in 1988.

Figure 3. Location of wells where hydrogeophysical datasets were collected, including cross-borehole electrical resistivity data (FW124 and FW125), water level data (SG002 in the saturated zone, and FW117 in an intermittently perched zone), and multilevel sampling geochemistry data (FW120). Note the approximate location of the drainage ditch relative to these wells. Surface electrical resistivity and crosshole seismic datasets were also collected; while they were not considered in this study, their locations are noted for reference.

Figure 4. (a) Measured rainfall rate for the time period considered in this study, with a solid black line showing the rate and a dashed red line showing cumulative rainfall, (b) measured water level in the drainage ditch next to the site. Days 98 to 365 of 2008 correspond to April through December.

Figure 5. Water level data for wells in the saturated zone (FW117) and in an intermittently perched zone (SG002). SG002 contains water only when the depth to the water level is less than 2.6 m (i.e., the well is dry when the water level is at 2.6 m).

Figure 6. Nitrate concentration profiles from multi-level sampling well FW120 (a) measured on six days of the year 2008 (as noted in the legend), (b) obtained for day 343 using linear and nearest-neighbor interpolation of the measurements, and (c) estimated for day 343 in the inversion procedure (described in Section 4.3).

Figure 7. Electrical resistivity grid showing (a) the electrodes for one current dipole (blue line) and the corresponding measurement dipoles (red lines). An additional 19 current dipoles at different depths are also included in the study, each with a different set of measurement dipoles, giving 581 measurements per survey. All the considered current dipoles and possible measurement dipoles are depicted in (b). In total we consider two surveys from December 2008.

Figure 8. (a) Conceptual model showing main geological layers, recharge sources (precipitation and drainage ditch water), water tables in an intermittently perched water body and the saturated zone, and two measurement wells; (b) 1D HM grid that accounts for vertical flow in the fill and Saprolite layers, and horizontal outflow in the transition zone to a fixed-pressure boundary; (c) 2D HM grid with outflow in the transition zone to a fixed-hydrostatic-pressure boundary; (d) example of output from 2D HM with overlapping 2D GM grid. The location of the electrodes used by the GM to simulate electrical resistivity measurements are shown in (c) and (d).

Figure 9. For Case A in Section 4.3.1, measured and simulated (a) water levels in the perched zone well (SG002), (b) water levels in the saturated zone well (FW117), and (c) nitrate concentrations at three sampling depths in FW120 as a function of time. The simulated results

were obtained using the parameters estimated by inversion using the coupled hydrogeochemical-geophysical model (See Tables 1 and 2).

Figure 10. For Case B in Section 4.3.2, measured and simulated (a) water levels in the perched zone well (SG002), (b) water levels in the saturated zone well (FW117), and (c) nitrate concentrations at the six sampling depths in FW120 as a function of time. The simulated results were obtained using the parameters estimated by inversion using the coupled hydrogeochemical-geophysical model (See Tables 1 and 2).

Figure 11. Sensitivity of the simulated nitrate concentration evolution to the shape of the profile used for initialization at day 343. The results of three simulations are shown, with the only difference in input parameters being the initial profile of nitrate concentration, as determined by linear or nearest-neighbor interpolation (Figure 6b) or by the result of the inversion procedure for Case B (Figure 6c). Both of the interpolated profiles honor the geochemistry data at the sampling locations.

Figure 12. Simulated water saturation for parameters obtained by inversion in Case B (Section 4.3.2) (a) at day 345 and simulated nitrate concentration at (b) day 345 and (c) 354, corresponding to the times of the electrical resistivity surveys, and at (d) day 362.

Figure 13. Shape of the objective function in the vicinity of the estimates of petrophysical parameter *m* of Archie's law (Equation 2) for the different regions defined in (a) Case C.1, (b) Case C.2, (c) Case C.3, and (d) Case C.4. For each curve, the specified parameter is varied and

the objective function is calculated, while any remaining parameters are fixed at the values previously estimated by inversion (shown with symbols). Details of the inversions are given in Tables 1, 2, and 3 and described in Section 4.3.3.

Figure 14. Shape of the objective function in the vicinity of the estimates of petrophysical parameters (a) σ_s for the combined fill and Saprolite layer and for the transitions zone, (b) R_1 and (c) R_2 for Case C.5. For each curve, the specified parameter is varied and the objective function is calculated, while the remaining parameters are fixed at the values previously estimated by inversion (shown with symbols). Details of the inversions are given in Tables 1, 2, and 3 and described in Section 4.3.3.

Figure 15. Measured (red) and simulated (black) electrical resistance values obtained with the parameters estimated by inversion of an electrical resistivity dataset for day 345 for (a) Case C.2 in Section 4.3.3 and (b) Case C.5 in Section 4.3.3. In each subplot, the measurement dipoles are shown corresponding to a single current dipole (CD 1 is the deepest current dipole, CD 20 is the shallowest; see Figure 7). The code used in this study automatically orders the electrodes for each dipole to give positive resistance values, thus allowing for the log transform of the data to be used in the inversion.

Figure 16. (a) Measured (red) and simulated (black) electrical resistance values at two survey times (days 345 and 354), obtained using the parameters estimated by coupled inversion of the hydrological datasets and electrical resistivity datasets (Case D.1), as is described in Section 4.3.4. (b) Simulated electrical resistance values at days 345 and 365, which corresponds to 11

days after the last electrical resistivity dataset was actually collected (at day 354). In each subplot, the measurement dipoles are shown corresponding to a single current dipole (CD 1 is the deepest current dipole, CD 20 is the shallowest; see Figure 7). The code used in this study automatically orders the electrodes for each dipole to give positive resistance values, thus allowing for the log transform of the data to be used in the inversion.

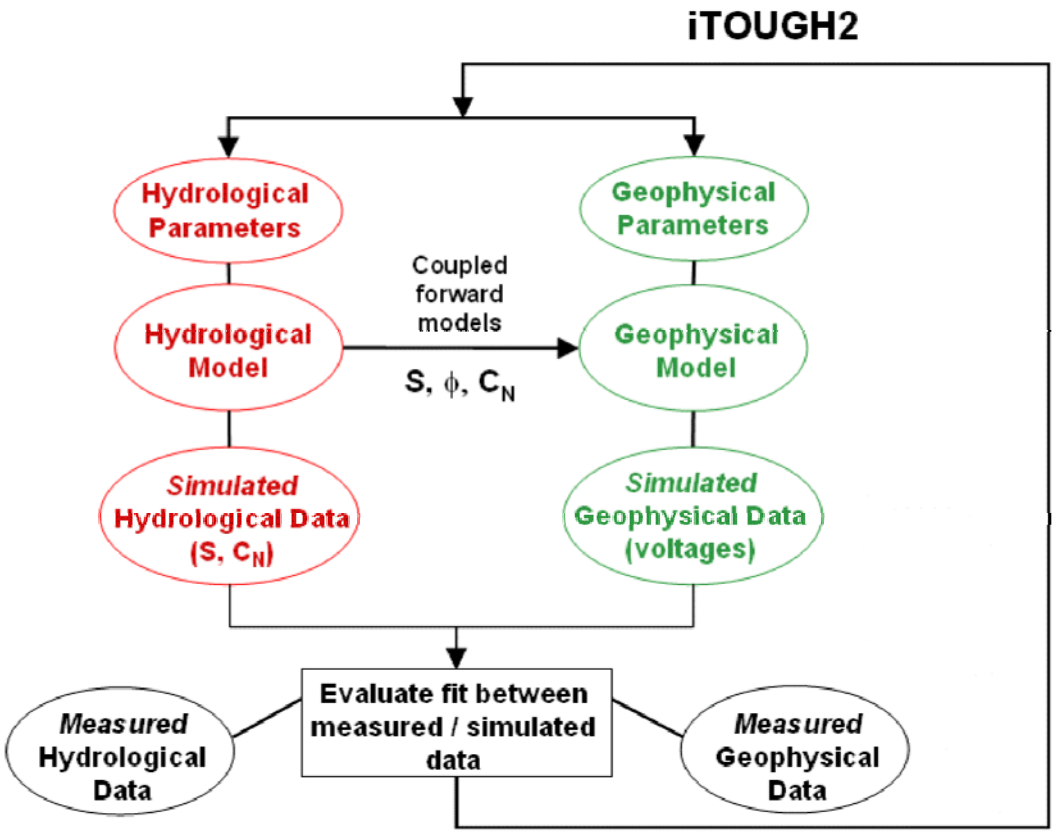
iTOUGH2
Hydrological Parameters
Geophysical Parameters
Coupled forward models
Hydrological Model
Geophysical Model
S, ϕ, C_N
Simulated Hydrological Data (S, C_N)
Simulated Geophysical Data (voltages)
Evaluate fit between measured / simulated data
Measured Hydrological Data
Measured Geophysical Data

Figure 1.

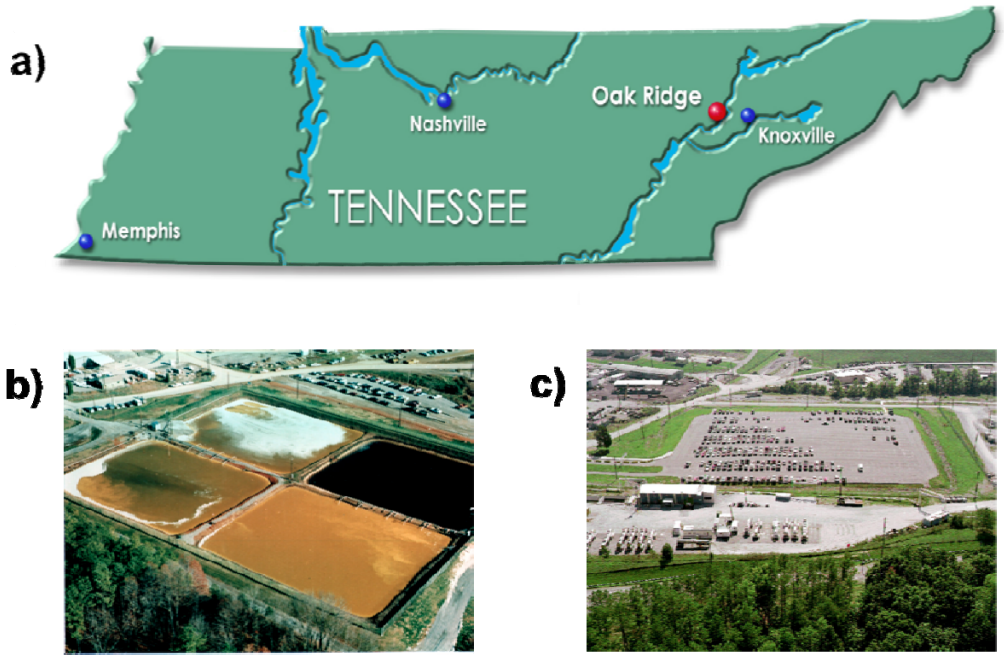

Figure 2.

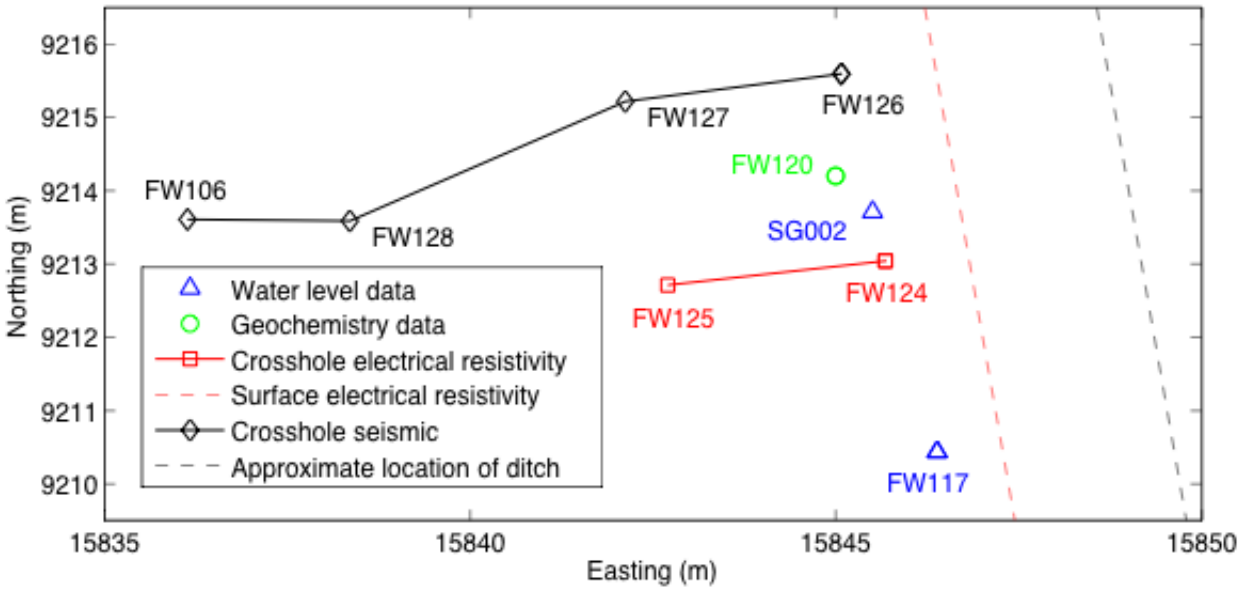
9216
9215
9214
9213
9212
9211
9210
Northing (m)
15835
15840
15845
15850
Easting (m)
FW106
FW128
FW127
FW126
FW120
SG002
FW125
FW124
FW117
Water level data
Geochemistry data
Crosshole electrical resistivity
Surface electrical resistivity
Crosshole seismic
Approximate location of ditch

Figure 3.

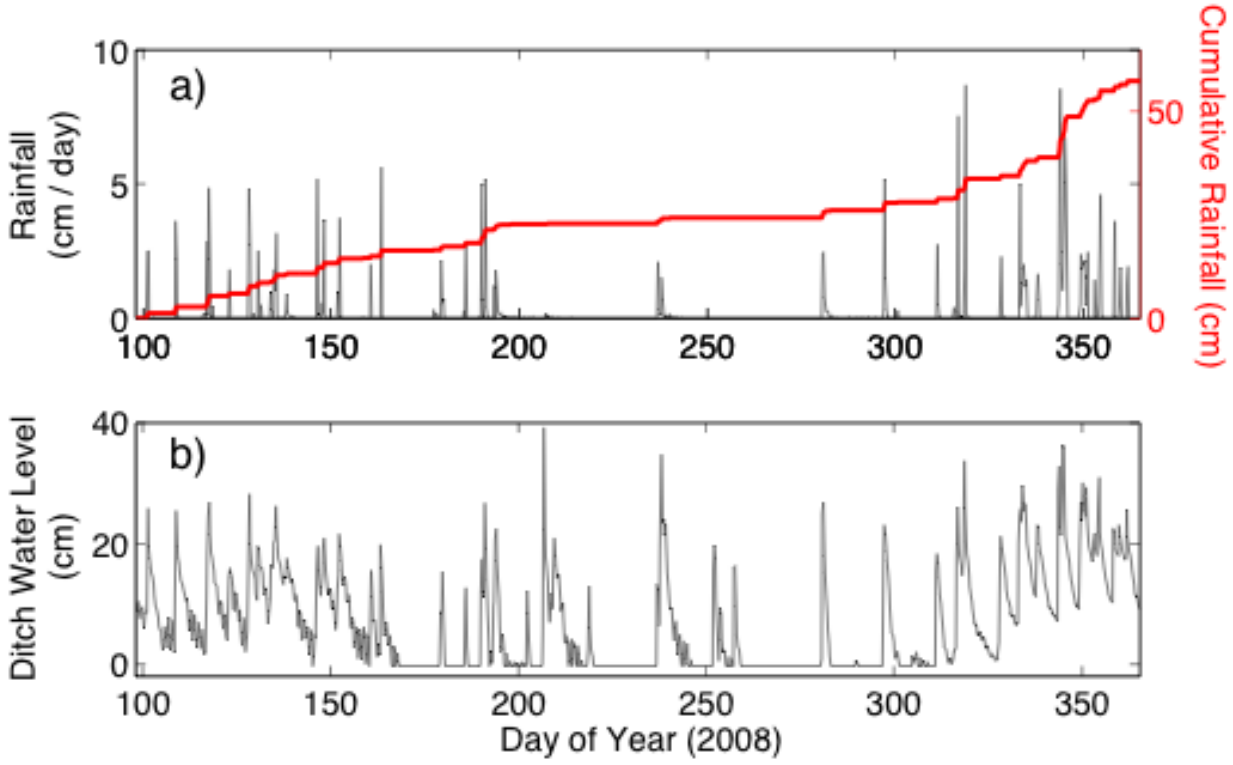
a)
b)
Rainfall
(cm / day)
Cumulative Rainfall (cm)
Ditch Water Level
(cm)
Day of Year (2008)
10
5
0
50
0
40
20
0
100
150
200
250
300
350

Figure 4.

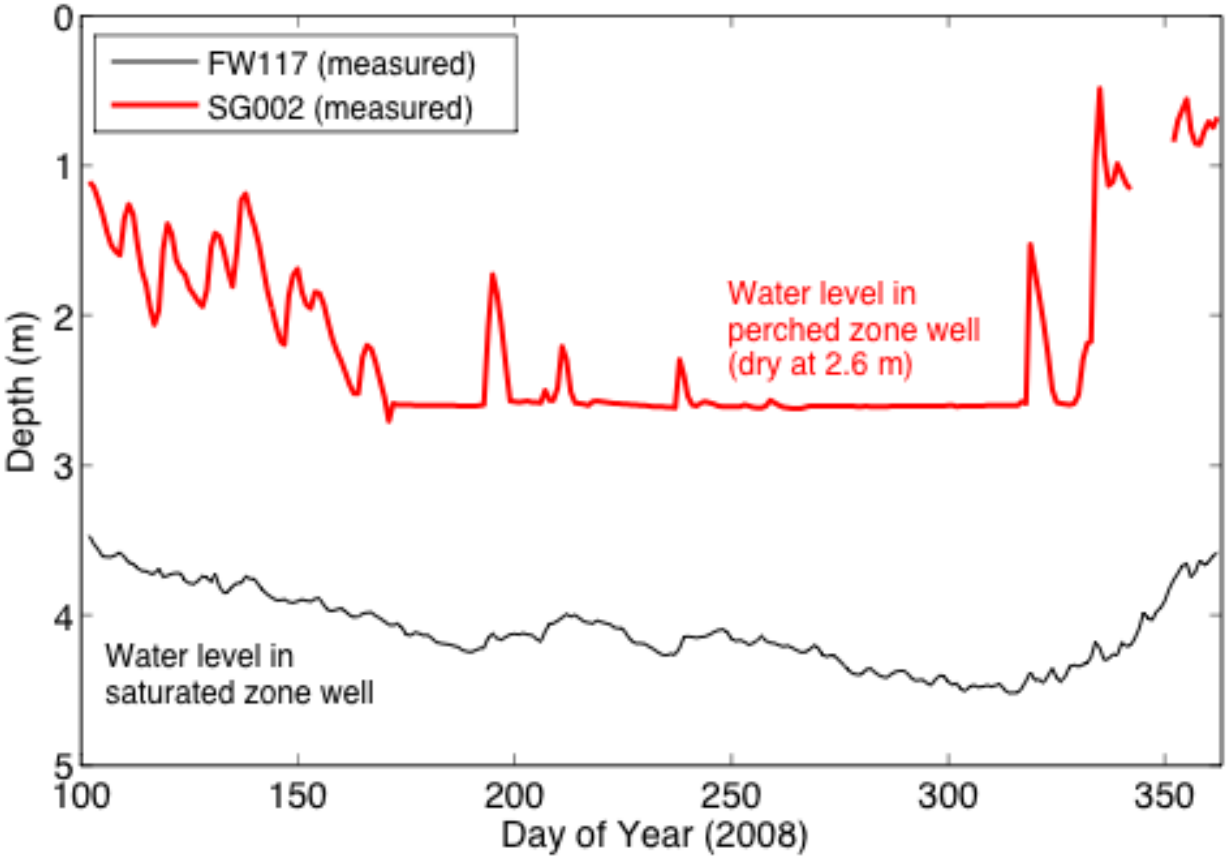
FW117 (measured)
SG002 (measured)
Water level in
perched zone well
(dry at 2.6 m)
Water level in
saturated zone well
Depth (m)
Day of Year (2008)
0
1
2
3
4
5
100
150
200
250
300
350

Figure 5.

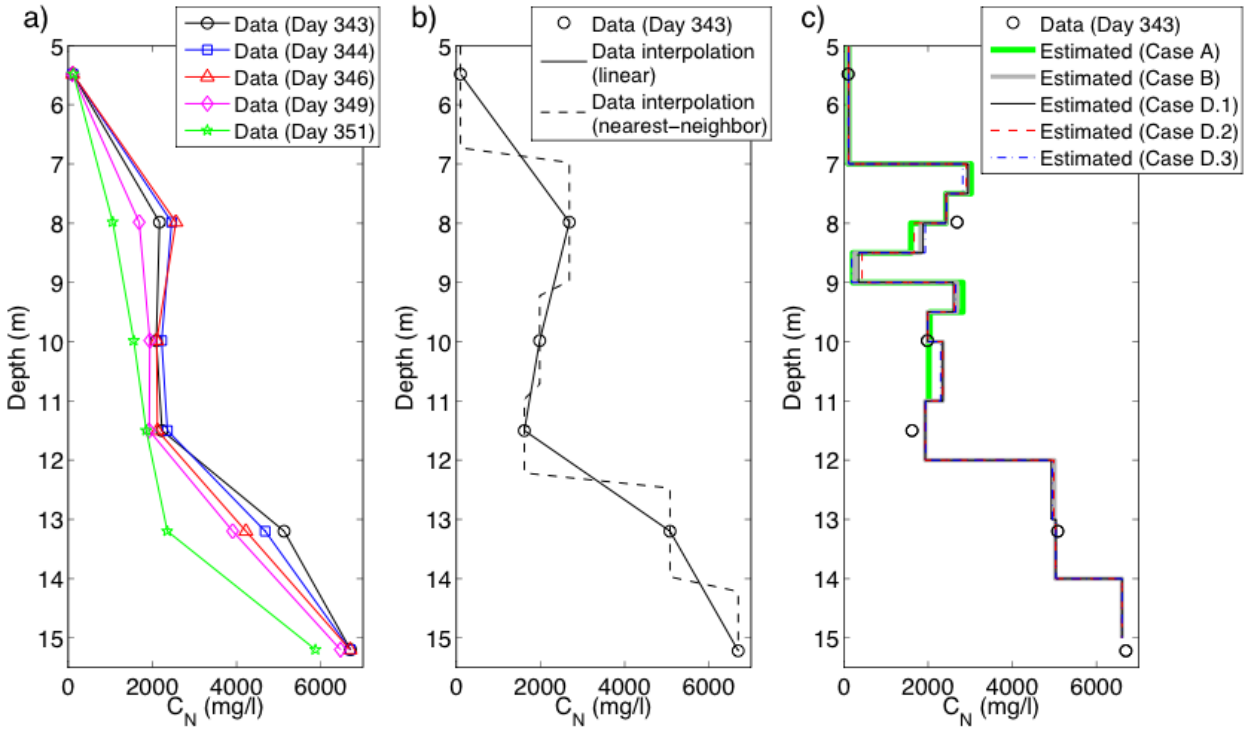
a)
Data (Day 343)
Data (Day 344)
Data (Day 346)
Data (Day 349)
Data (Day 351)
Depth (m)
C_N (mg/l)
b)
Data (Day 343)
Data interpolation (linear)
Data interpolation (nearest−neighbor)
Depth (m)
C_N (mg/l)
c)
Data (Day 343)
Estimated (Case A)
Estimated (Case B)
Estimated (Case D.1)
Estimated (Case D.2)
Estimated (Case D.3)
Depth (m)
C_N (mg/l)

Figure 6.

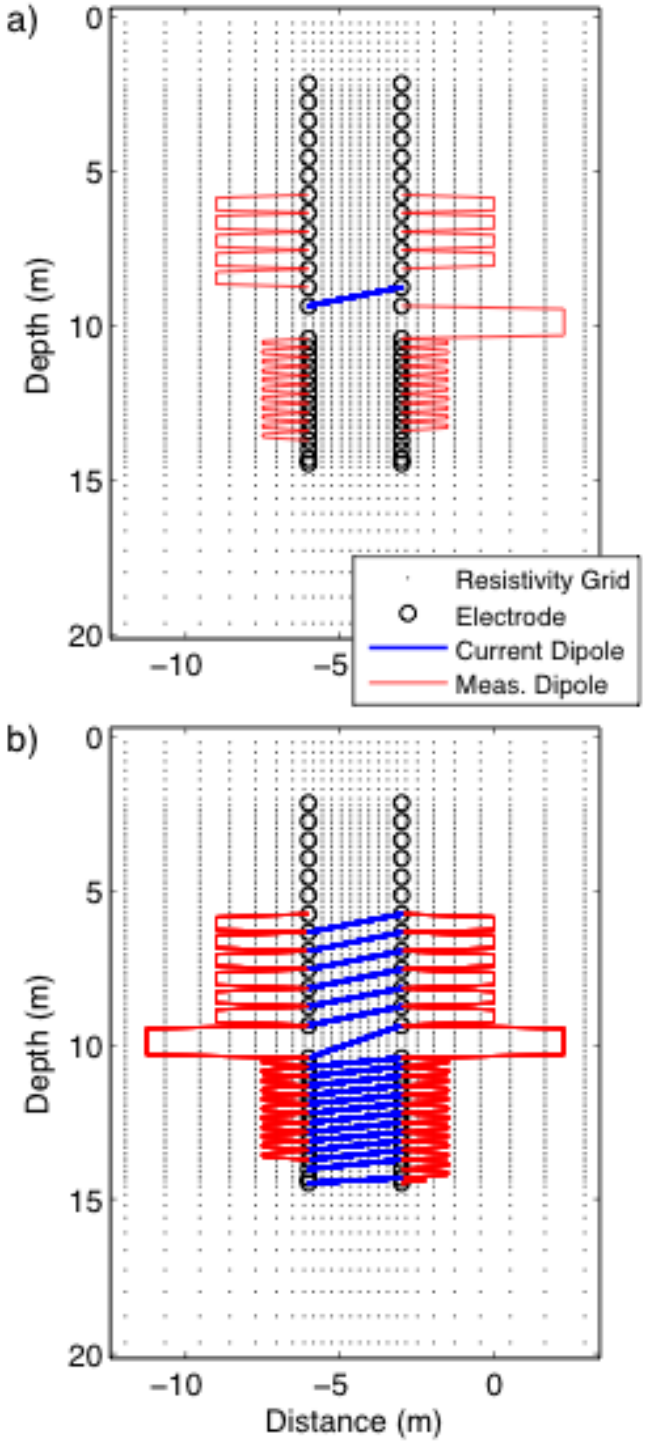
a)
b)
Depth (m)
Distance (m)
0
5
10
15
20
−10
−5
0
Resistivity Grid
Electrode
Current Dipole
Meas. Dipole

Figure 7.

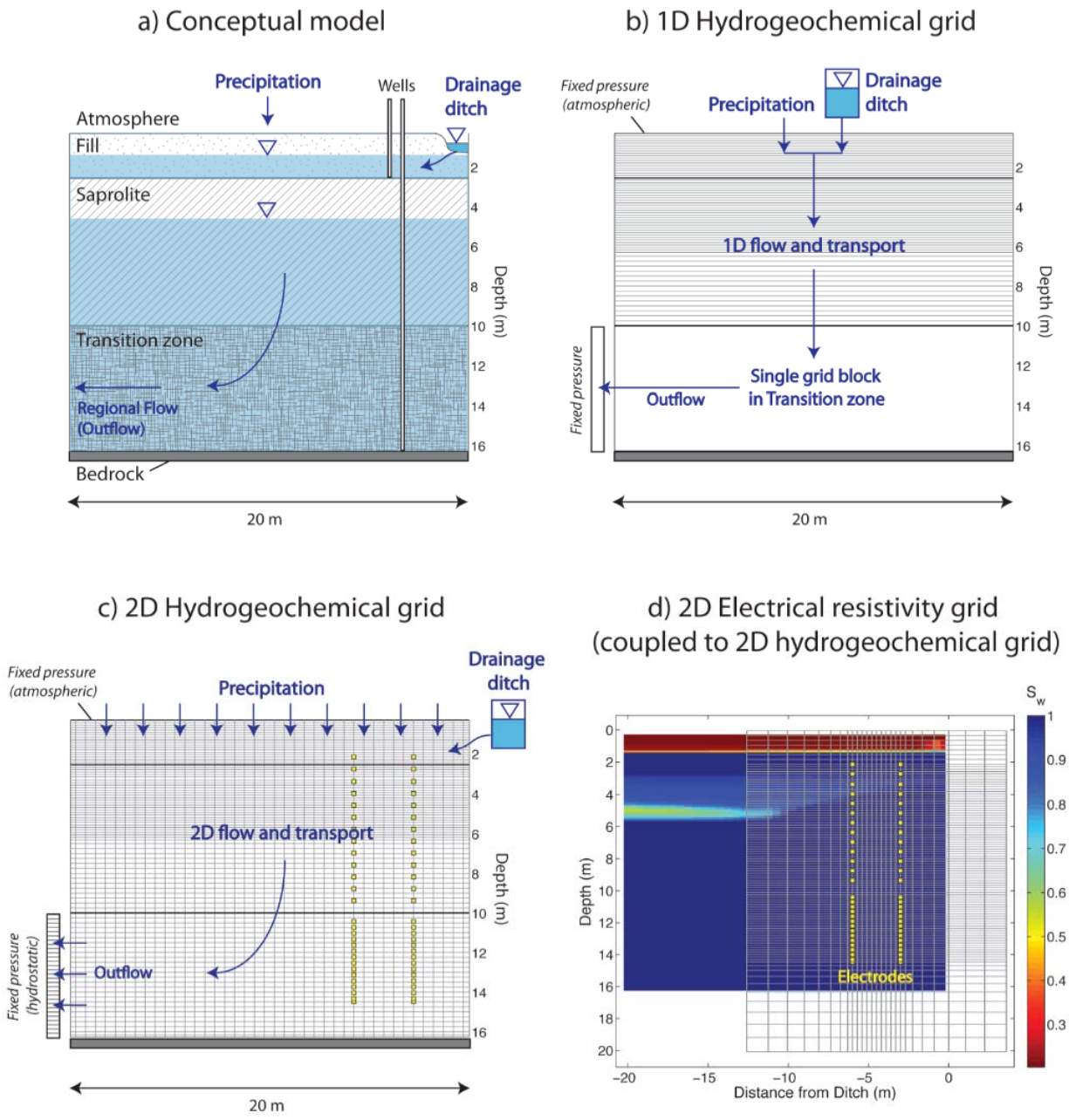
a) Conceptual model
Precipitation
Wells
Drainage ditch
Atmosphere
Fill
Saprolite
Transition zone
Regional Flow (Outflow)
Bedrock
Depth (m)
20 m
b) 1D Hydrogeochemical grid
Fixed pressure (atmospheric)
Precipitation
Drainage ditch
1D flow and transport
Fixed pressure
Outflow
Single grid block in Transition zone
Depth (m)
20 m
c) 2D Hydrogeochemical grid
Fixed pressure (atmospheric)
Precipitation
Drainage ditch
2D flow and transport
Fixed pressure (hydrostatic)
Outflow
Depth (m)
20 m
d) 2D Electrical resistivity grid (coupled to 2D hydrogeochemical grid)
S_w
Depth (m)
Electrodes
Distance from Ditch (m)

Figure 8.

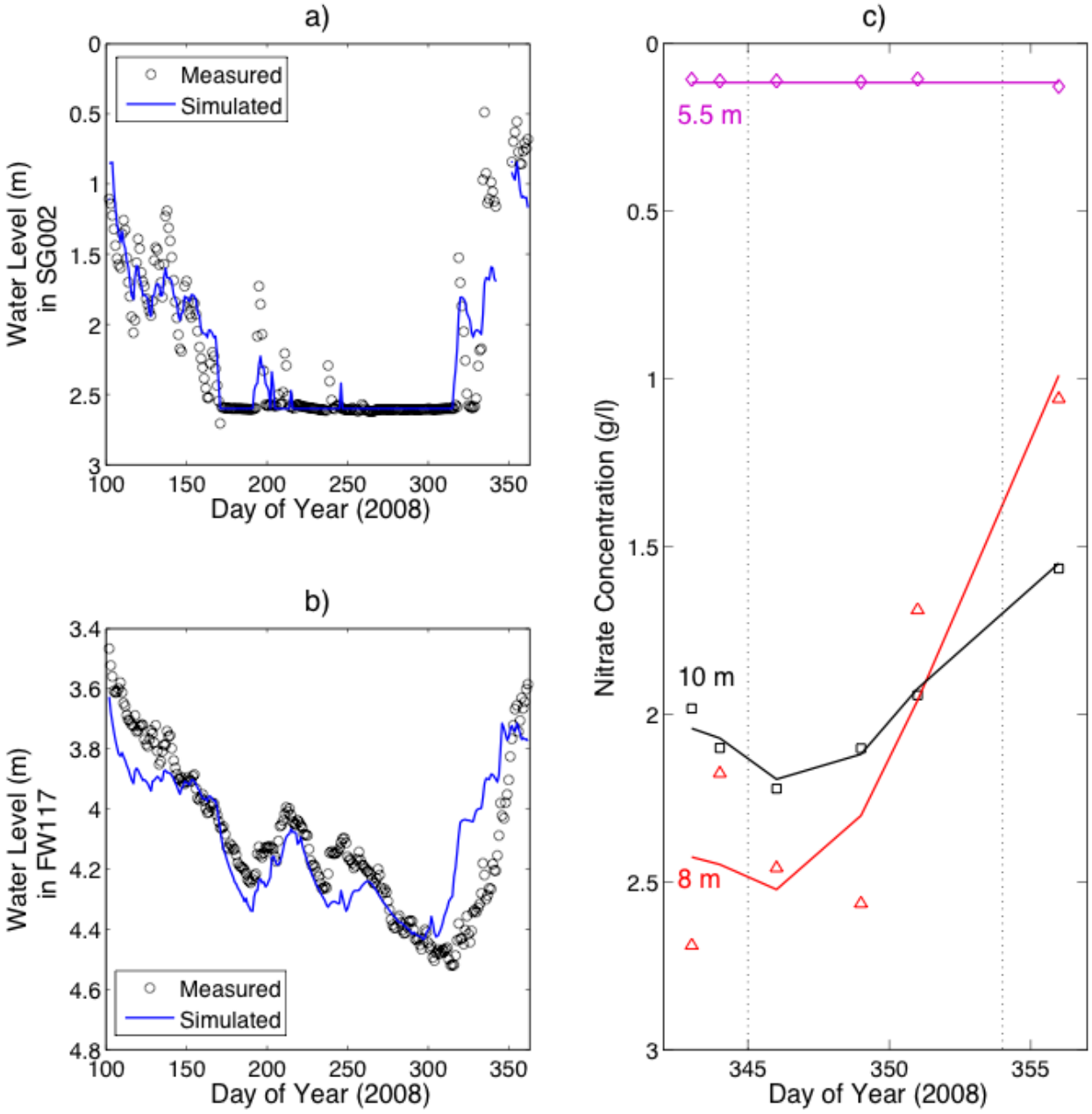
a)
Measured
Simulated
Water Level (m) in SG002
Day of Year (2008)
b)
Water Level (m) in FW117
Measured
Simulated
Day of Year (2008)
c)
5.5 m
10 m
8 m
Nitrate Concentration (g/l)
Day of Year (2008)

Figure 9.

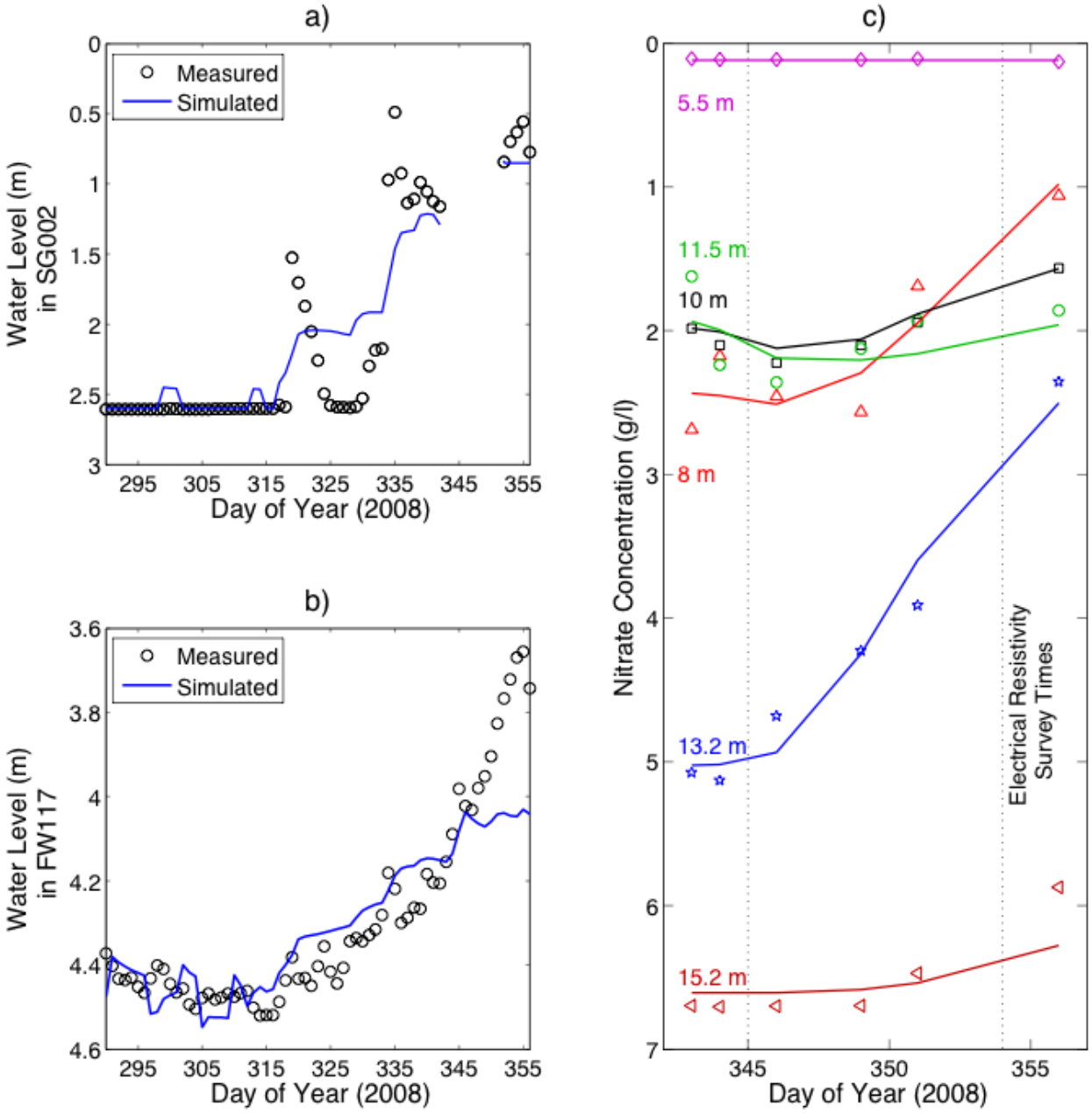
a)
Measured
Simulated
Water Level (m) in SG002
Day of Year (2008)
b)
Measured
Simulated
Water Level (m) in FW117
Day of Year (2008)
c)
5.5 m
11.5 m
10 m
8 m
13.2 m
15.2 m
Nitrate Concentration (g/l)
Electrical Resistivity Survey Times
Day of Year (2008)

Figure 10.

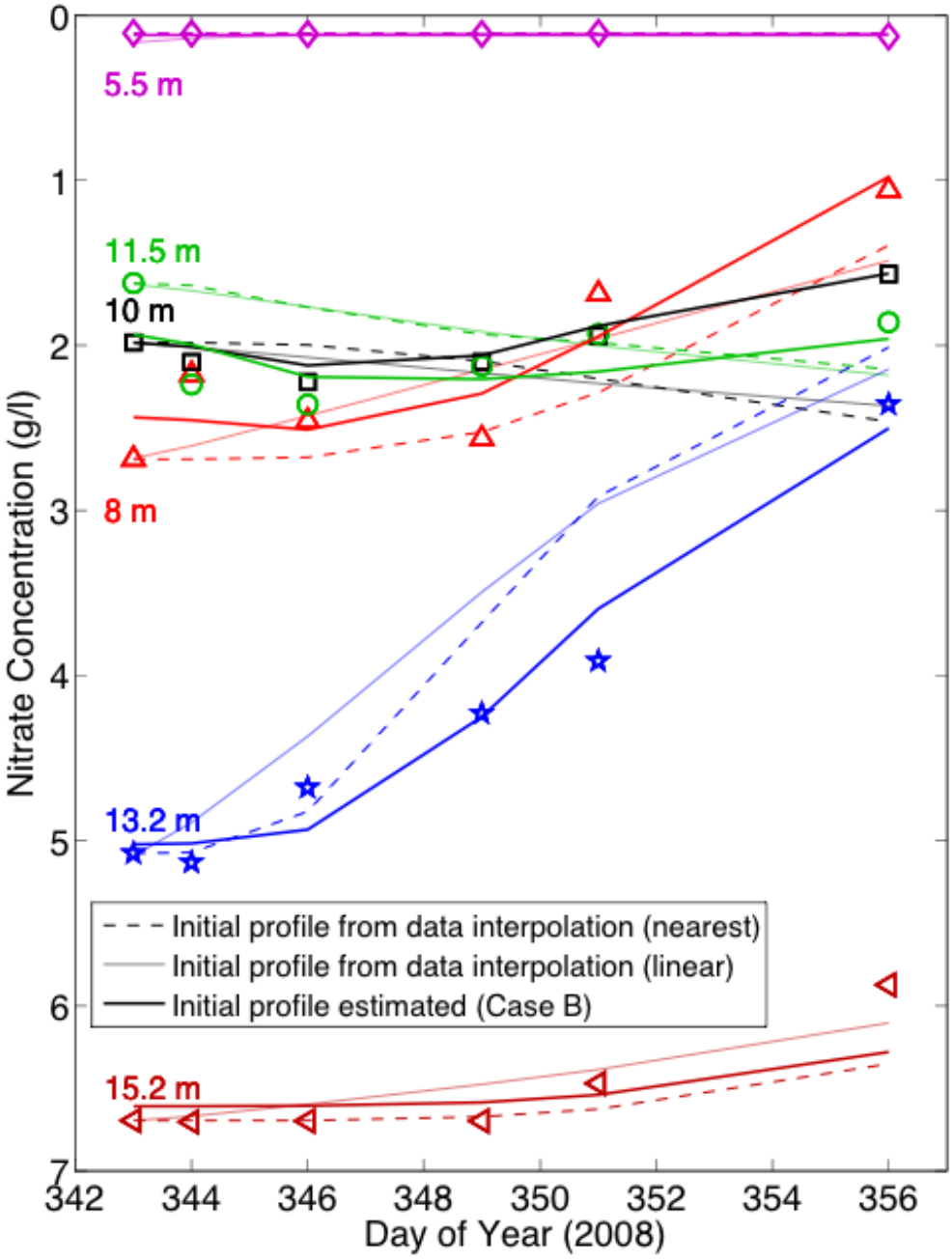
0
1
2
3
4
5
6
7
342
344
346
348
350
352
354
356
Day of Year (2008)
Nitrate Concentration (g/l)
5.5 m
11.5 m
10 m
8 m
13.2 m
15.2 m
Initial profile from data interpolation (nearest)
Initial profile from data interpolation (linear)
Initial profile estimated (Case B)

Figure 11.

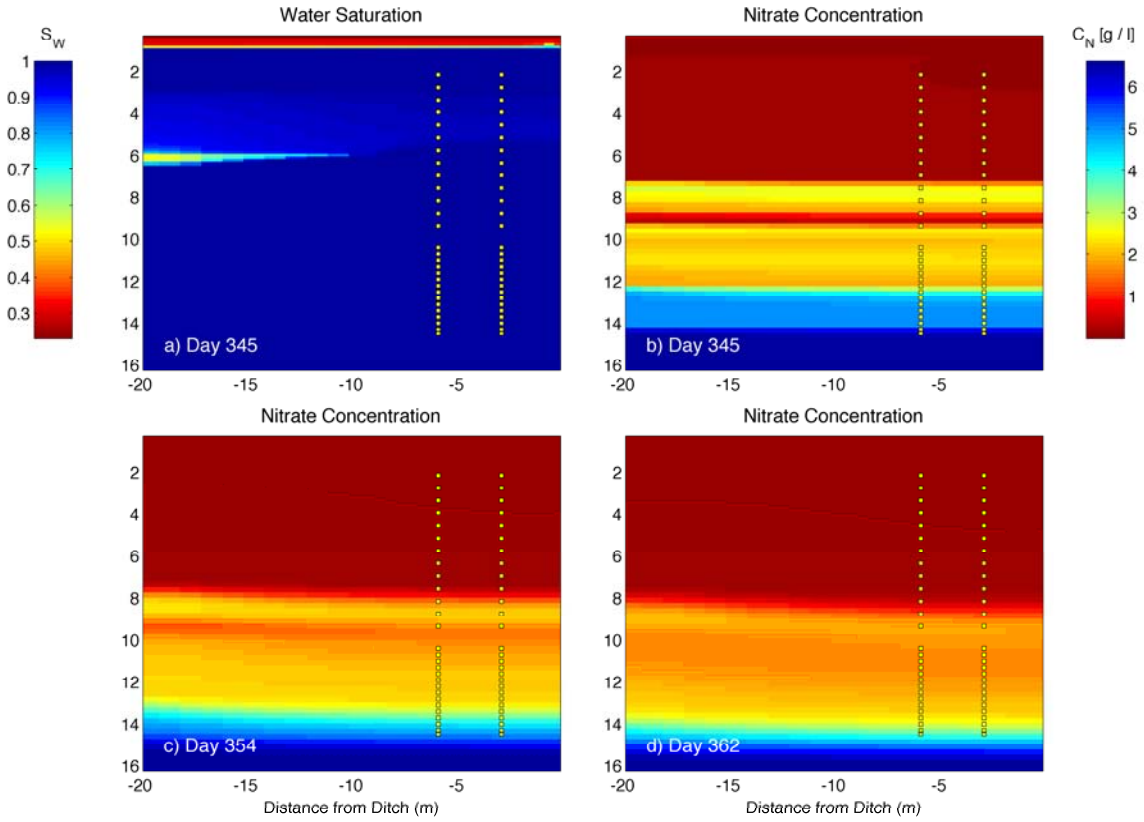
Water Saturation
Nitrate Concentration
S_W
C_N [g / l]
a) Day 345
b) Day 345
c) Day 354
d) Day 362
Nitrate Concentration
Nitrate Concentration
Distance from Ditch (m)
Distance from Ditch (m)

Figure 12.

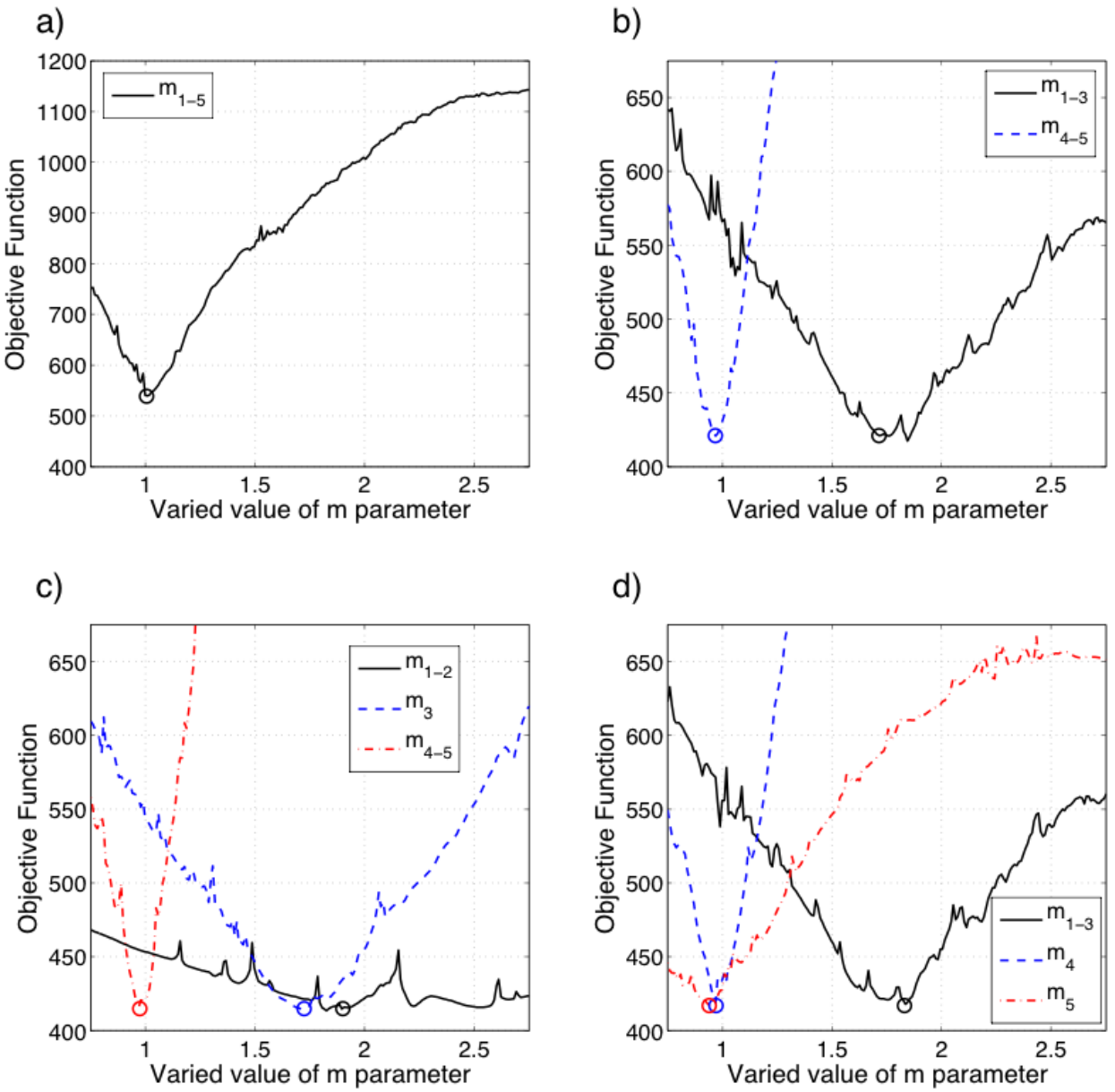
a)
b)
c)
d)
Objective Function
Varied value of m parameter
m1–5
m1–3
m4–5
m1–2
m3
m4
m5

Figure 13.

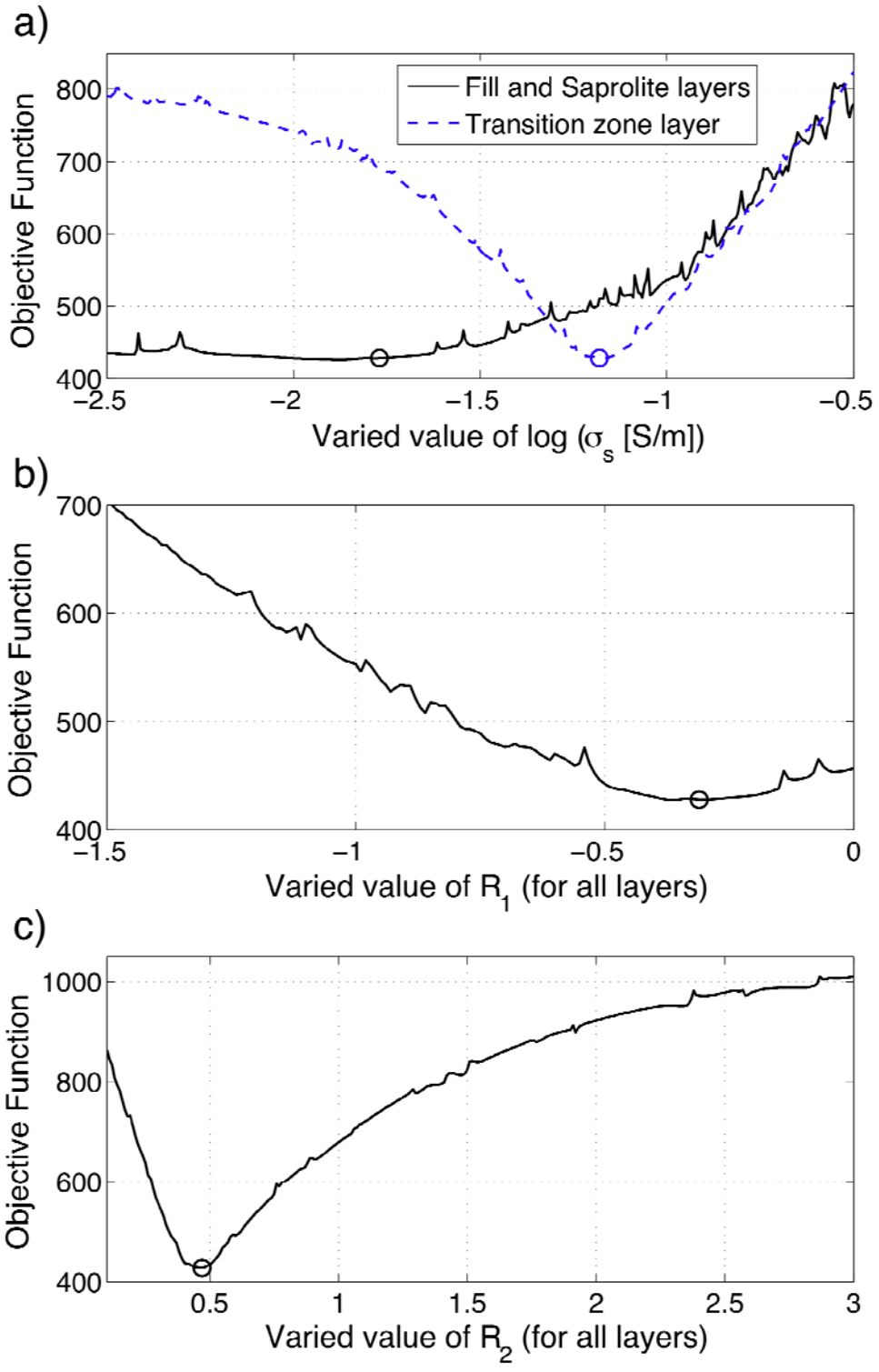
a)
Fill and Saprolite layers
Transition zone layer
Objective Function
800
700
600
500
400
−2.5
−2
−1.5
−1
−0.5
Varied value of log (σs [S/m])
b)
Objective Function
700
600
500
400
−1.5
−1
−0.5
0
Varied value of R1 (for all layers)
c)
Objective Function
1000
800
600
400
0.5
1
1.5
2
2.5
3
Varied value of R2 (for all layers)

Figure 14.

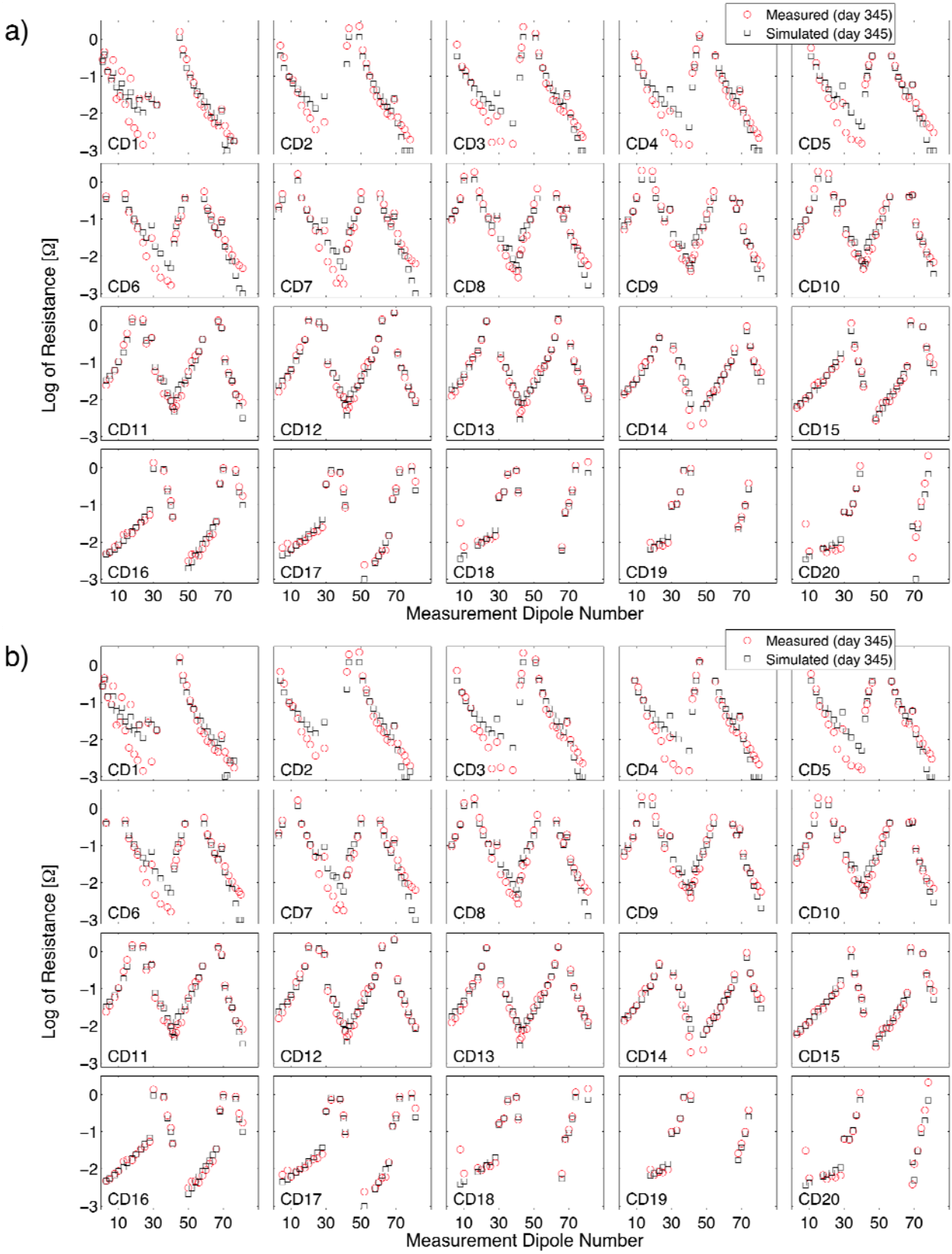
a)
b)
Measured (day 345)
Simulated (day 345)
Log of Resistance [Ω]
Measurement Dipole Number
CD1
CD2
CD3
CD4
CD5
CD6
CD7
CD8
CD9
CD10
CD11
CD12
CD13
CD14
CD15
CD16
CD17
CD18
CD19
CD20

Figure 15.

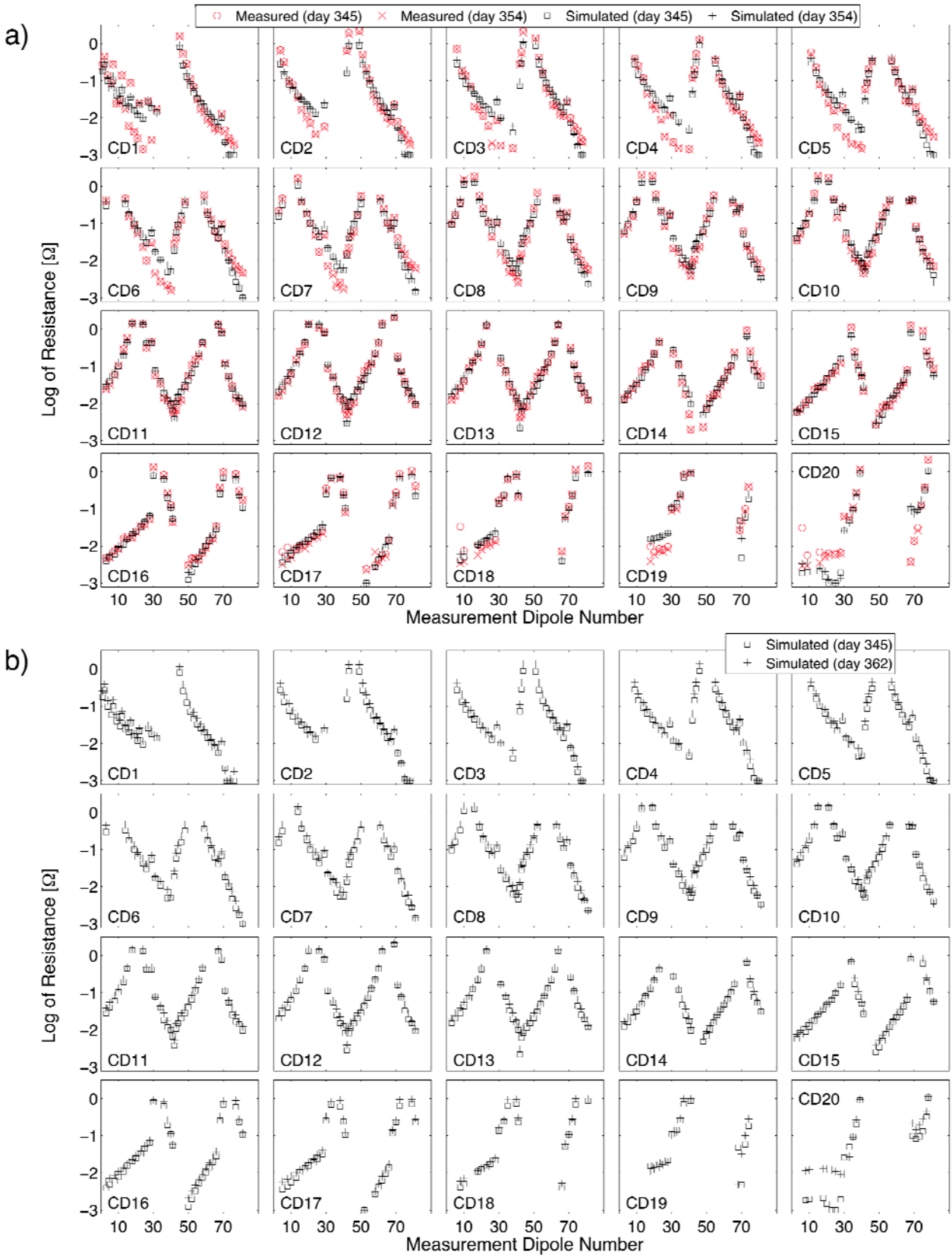
a)
Measured (day 345)
Measured (day 354)
Simulated (day 345)
Simulated (day 354)
Log of Resistance [Ω]
CD1
CD2
CD3
CD4
CD5
CD6
CD7
CD8
CD9
CD10
CD11
CD12
CD13
CD14
CD15
CD16
CD17
CD18
CD19
CD20
Measurement Dipole Number
b)
Simulated (day 345)
Simulated (day 362)
Log of Resistance [Ω]
Measurement Dipole Number

Figure 16.

DISCLAIMER